

TECHNICAL NOTE

D-689

THE FLOW FIELD OVER BLUNTED FLAT PLATES AND ITS
EFFECT ON TURBULENT BOUNDARY-LAYER GROWTH
AND HEAT TRANSFER AT A MACH NUMBER OF 4.7

By Thorval Tendeland, Helmer L. Nielsen,
and Melvin J. Fohrman

Ames Research Center
Moffett Field, Calif.

NATIONAL AERONAUTICS AND SPACE ADMINISTRATION
WASHINGTON

February 1961

L

NATIONAL AERONAUTICS AND SPACE ADMINISTRATION

TECHNICAL NOTE D-689

THE FLOW FIELD OVER BLUNTED FLAT PLATES AND ITS
EFFECT ON TURBULENT BOUNDARY-LAYER GROWTH
AND HEAT TRANSFER AT A MACH NUMBER OF 4.7

By Thorval Tendeland, Helmer L. Nielsen,
and Melvin J. Fohrman

SUMMARY

Surface pressures, impact and static pressure distributions in the flow field over the plate, and local heating rates were measured on a flat plate with various leading-edge diameters. The tests were conducted at a Mach number of 4.7 and a free-stream Reynolds number of 3.8×10^6 per foot.

It was found that the shape of the shock wave indicated the existence of an outward deflection of the flow over the plate. The flow deflection caused an outward deflection of the shock-wave asymptote of approximately 3° ; this angle is much larger than the shock-wave angle calculated including boundary-layer growth. The Mach number distributions in the shear layer evaluated from pitot and static pressure surveys agreed with predictions based on shock-wave shape. The predicted turbulent heat-transfer coefficients for the blunted flat plates agreed with the measured heat-transfer coefficients. A comparison between the measured heat-transfer coefficients for the blunted flat plates and the calculated coefficients for a sharp leading-edged plate indicated that the coefficients were highest near the leading edge of the most blunted plate. The measured heat-transfer coefficients dropped to approximately 80 percent of the sharp-plate values at a considerable distance from the leading edge for all of the blunted flat plates.

INTRODUCTION

Use of blunted aerodynamic shapes is a well recognized technique for reducing aerodynamic heating at hypersonic speeds. The flow field and surface pressure phenomena associated with blunted shapes differ considerably from the flow field associated with sharp, slender bodies at Mach numbers above about 5. The flow over a flat plate with a blunted

1

leading edge has been considered in a number of theoretical and experimental studies. One of the earliest considerations of the problem was in reference 1 where it was observed that at $M_\infty = 6.9$, the pressure on the forward wedge surface of an airfoil was not constant as classical inviscid flow theory would predict. It was suggested that the growth of the boundary layer on the surface created, in effect, a curved surface which caused the observed pressure distribution.

Following this initial work a number of analytical papers were published which attempted to calculate the flow field caused by this viscous-inviscid interaction. They can be divided into two classes:

1. Those which applied the boundary-layer equations to the whole region between the plate and the shock wave (e.g., refs. 2-5).
2. Those which divided the region between the shock wave and the plate into a boundary layer and an inviscid region (e.g., refs. 6-10).

Experimental studies of hypersonic flow of helium over blunted flat plates indicated that the pressures on the surface were considerably higher than those predicted by the viscous-inviscid flow interactions. It was found for example in reference 11 that the leading-edge thickness had an important influence on surface pressures. Blast-wave theory has been used to predict the effect of leading-edge bluntness on surface pressures but has been able to account for leading-edge blunting effects only when viscous effects are small as noted in references 12, 13, and 14. In reference 15 pressure distributions on flat plates with various leading-edge configurations were correlated by assuming a linear combination of the boundary-layer parameter given in reference 7 and the blast-wave parameter given in reference 14. The investigations of references 12 through 15 were mainly concerned with the measurement and correlation of surface pressures and shock-wave shapes.

The purpose of this investigation is to study the entire flow field over blunted flat plates. It is hoped that the results of this study will serve as a basis for the development of methods for predicting heat-transfer rates downstream from the blunt leading edge for both laminar and turbulent boundary layers. Surface pressures, impact and static pressure distributions in the flow field over the plate surface, and local heating rates were measured on a flat plate having various leading-edge diameters.

SYMBOLS

A	cross-sectional area of a stream tube entering shock wave (see fig. 3(b))
a	cross-sectional area of stream tube behind shock wave (see fig 3(b))
$\left(\frac{A^*}{A}\right)_M$	isentropic area contraction ratio from Mach number M to Mach number 1.0
B	$\left(\frac{A^*}{A}\right)_{M_\infty} \left(\frac{P_\infty}{P}\right)_c$
b	$\left[\frac{0.865}{M_e^2} \frac{T_w}{T_\infty} + 0.166(\gamma - 1) \right] \gamma$
C_D	drag coefficient of cylinder
C_f	average skin-friction coefficient, $\frac{1}{x} \int_0^x c_f dx$
C_w	constant in linear relation between viscosity and temperature, $\frac{\mu_w T_e}{\mu_e T_w}$
c	$0.112 (C_D)^{2/3}$ (for air)
c_f	local skin-friction coefficient, $\frac{\mu(du/dy)}{(1/2)\rho u^2}$
c_p	specific heat at constant pressure, Btu/lb, °R
d	leading-edge plate thickness, in.
H	boundary-layer shape parameter $\frac{\delta^*}{\theta}$
h	heat-transfer coefficient, Btu/sec, ft ² , °R
I	blast wave pressure term, $\frac{M_\infty^2}{(x/d)^{2/3}}$
k	thermal conductivity, Btu/sec, ft ² , °R/ft

L	distance along body from sharp leading edge, ft (see fig. 1)
M	Mach number
P	stagnation pressure, lb/sq ft
Pr	Prandtl number, $\frac{\mu c_p}{k}$
p	static pressure, lb/sq ft
q	local heat-transfer rate per unit area, Btu/ft ² sec
R _d	Reynolds number, $\frac{u_e \rho_e d}{\mu_e}$
R _x	Reynolds number, $\frac{u_e \rho_e x}{\mu_e}$
R _∞	Reynolds number, $\frac{u_\infty \rho_\infty x}{\mu_\infty}$
R _θ	Reynolds number, $\frac{u_e \rho_e \theta}{\mu_e}$
r	leading-edge radius, in.
St	Stanton number, $\frac{h}{\rho_e u_e c_p}$
T	temperature, °R
t	time, sec
u	air velocity, ft/sec
X	coordinate length in stream direction, ft (see fig. 3(b))
x ₀	distance from foremost point of detached shock to intercept of its asymptote on x axis, ft (see fig 3(b))
x	distance along the body from plane tangent to leading edge, ft
Y	coordinate length normal to stream direction, ft (see fig. 3(b))
y	distance normal to plate surface, ft (see fig. 3(b))
β	defined in figure 3(b)

γ	ratio of specific heats
Δ	detachment distance, ft (see fig. 3(b))
δ	boundary-layer thickness, ft
δ^*	boundary-layer displacement thickness, ft
η	angle between sonic line and normal to free-stream direction, deg (see fig. 3(b))
θ	boundary-layer momentum thickness, ft
λ_d	wedge half-angle for which shock becomes detached, deg (see fig. 3(b))
λ_s	angle of streamline relative to x axis, deg (see fig. 3(b))
μ	coefficient of viscosity, lb/sec ft
ρ	density of air, lb/cu ft
ρ_m	density of model material, lb/cu ft
τ_m	thickness of model material, ft
ϕ	local inclination of detached shock relative to x axis, deg (see fig. 3(b))
\bar{X}	interaction parameter

Subscripts

aw	conditions at surface for zero heat transfer
c	centroid of stream tube passing sonic line
e	local stream condition at outer edge of boundary layer
M	Mach angle
m	model material
S	sonic point on detached shock wave
SB	sonic point on body
sw	conditions at the shock wave
s	conditions along sonic line

t	effective start of turbulent boundary layer
tb	theoretical values for blunt leading-edged plates
ts	theoretical values for sharp leading-edged plates
w	conditions at surface of model
∞	undisturbed free-stream conditions
1	discrete point in the shear layer

Superscripts

n	exponent which depends on the temperature-ratio variation of viscosity
()'	conditions at which incompressible flow relations must be evaluated in order to represent compressible flow

DESCRIPTION OF EQUIPMENT AND TEST METHOD

Wind Tunnel

The tests were conducted in the Ames 10-Inch Heat Transfer Wind Tunnel which is a variable-pressure, variable-temperature, continuous-flow type with a Mach number range from 3 to 5. A description of the wind tunnel can be found in reference 16. The conditions at which the wind-tunnel tests were performed were a free-stream Mach number of 4.7, which was determined from the ratio of the tunnel side-wall pressure (measured upstream of the shock wave of the body) to the reservoir pressure, a free-stream Reynolds number of 3.8×10^6 per foot, a stagnation pressure of 87 psia, and a stagnation temperature of 250° F.

Test Body

The body tested was a flat plate 10 inches wide by approximately 16 inches long and $3/4$ inch thick with four interchangeable circular leading-edge slugs as shown in figure 1. The plate spanned the full width of the wind-tunnel test section. It consisted of a stainless steel framework covered with a type 321 stainless steel sheet 0.125 inch thick on the bottom and 0.063 inch thick on top to form the testing surface. The center portion of the framework was channeled out to a depth of approximately $1/4$ inch and a width of 2-1/2 inches to minimize heat

conduction from the testing surface and to allow for the passage of thermocouple wires and pressure tubes. Great care was taken to keep the surface smooth and level. A profilometer record taken along the center line showed two scratches no greater than 50 microinches deep and the remaining deviations no greater than 5 microinches.

The test surface was instrumented with 11 pressure orifices 0.0135 inch in diameter distributed as shown in figure 1. Surface pressures were measured with a dibutylphthalate manometer. Temperatures were measured by 33 chromel-constantan thermocouples spot welded to the underside of the stainless steel skin. The first 11 were placed on the center line at stations corresponding to the locations of the pressure taps. The remainder were placed 0.57 inch in a spanwise direction from the center line. Number 36 B and S gage chromel and constantan wires were selected as the thermocouple materials because of their high thermoelectric potential.

To obtain a turbulent boundary layer over most of the plate it was necessary to use an artificial trip. Two strips of 1-50-D garnet paper, 3/8 inch wide, with most of the backing removed, were used for this purpose. They were cemented on the top surface 1/4 inch from the leading edge and 1/8 inch apart.

Boundary-Layer Survey Apparatus

Impact and static pressures were obtained throughout the flow region between the plate and the shock wave by probes mounted on a mechanically actuated apparatus which had three translational degrees of freedom (within limited ranges). The static pressure was measured with a long 1/16-inch-diameter ogive-shaped needle and the total pressure was measured with a 1/32-inch-diameter tube whose opening was flattened to approximately a 0.005-inch height. The survey apparatus was mounted in the side wall of the wind-tunnel test section and the probes were mounted on the end of a diamond-shaped strut which extended into the air stream. Probe position was determined by reading three counters which were connected to the drive mechanisms for the x, y, and z axes.

It was possible to obtain continuous plots of impact and static pressures against distance from the surface of the plate in the following manner. The pressure detected by the impact pressure probe was fed into a pressure cell of the unbonded strain gage type. This cell was calibrated at the beginning and end of each survey by means of a mercury manometer. The output from the pressure cell was fed into a function plotter where it was plotted continuously as the abscissa. The position of the ordinate was obtained from the vertical travel of the survey mechanism.

Heat-Transfer Measurements

The technique of transient temperature rise was used in the heat-transfer measurements. The output from the center line thermocouples was fed through an amplifier and differentiator. The temperature and temperature-time derivatives were recorded on a 50-channel oscillograph. The remainder of the thermocouples were connected directly to the oscillograph. All thermocouples were referenced to an ice bath.

The following experimental procedure was maintained during the test runs. The wind tunnel was operated at a stagnation temperature of 250° F until all parts of the test section were in thermal equilibrium and then the local recovery temperatures of the plate were recorded. Next, liquid nitrogen was injected upstream of the first throat to cool the plate to approximately 100° F below the recovery temperature. When the minimum temperature was reached, injection of the liquid nitrogen was suddenly stopped, and the temperatures and temperature-time derivatives were recorded on the oscillograph as the plate was aerodynamically heated.

REDUCTION OF DATA

Determining Heat-Transfer Rates

Local heat-transfer rates were evaluated from the oscillograph readings of temperature and the time rate of change of the temperature, by means of the following general heat balance equation:

$$\left. \begin{aligned} q_{\text{plate}} &= q_{\text{aerodynamic}} + q_{\text{tare}} \\ \text{or} \quad \rho_m \tau_m c_{p_m} \frac{dT_w}{dt} &= h(T_r - T_w) + q_{\text{tare}} \end{aligned} \right\} \quad (1)$$

The conduction losses in the spanwise direction were calculated from experimental data obtained from the thermocouples on either side of the model center line and were found to be negligible for the temperature gradients encountered during the tests.

The radiation and internal conduction losses were experimentally determined and are represented by the q_{tare} term. This term was obtained from readings of temperature and the time rate of change of this temperature for the cooled plate at the end of a run immediately after the wind tunnel had been shut down. The static pressure during this run was approximately the same as when the tunnel was running. The magnitude of q_{tare} was approximately 10 percent of the aerodynamic heating term ($q_{\text{aerodynamic}}$). The plate density in equation (1) was found

experimentally, and the specific heat of the skin and its variation with temperature were obtained from data published in reference 17.

The primary variables to be measured in equation (1) were the wall temperature and the time rate of change of this temperature. Temperatures were measured directly by the deflections of the galvanometer traces. The temperature rates were obtained by two methods: direct measurement of the galvanometer traces of the differentiator output, and measurement of temperature differences over small increments of time to determine an average slope by means of the ratio $\Delta T_w / \Delta t$. The differences noted between the two methods were random and did not exceed the experimental scatter.

Evaluating a Local Reynolds Number and Effective Length

The Reynolds number is customarily expressed in terms of a characteristic length. For a laminar boundary layer the characteristic length is the distance back from the leading edge of the body. For a turbulent boundary layer, with natural transition, the characteristic length is some lesser distance because the turbulent boundary layer grows at a much faster rate than the laminar boundary layer. When a turbulent boundary layer is induced artificially its characteristic length is not readily determined. The presence of a trip causes a loss of momentum in the boundary layer and a consequent thickening which cannot be correlated by using the geometric length of run of the boundary layer. Therefore an effective origin for turbulent flow is based on the measurement of the boundary-layer momentum thickness and its correlation with the skin-friction coefficient. The expression for the length of run from this origin to any point on the plate is given by

$$x = 84.0 R_\theta^{1.22} \left(\frac{T'}{T_e} \right)^{1.22n} \left(\frac{\mu_e}{\rho_e u_e} \right) \quad (2)$$

which is derived in appendix A. Using this equation is equivalent to determining the local skin-friction coefficient at a particular station and then calculating the length of run for a completely turbulent boundary layer which would produce that local skin-friction coefficient.

RESULTS AND DISCUSSION

Surface Pressure Distribution

The measured pressure on the plate surface for various leading-edge diameters as a function of the distance from the leading edge is shown in figure 2. The solid line in figures 2(a), (b), (c), and (d) represents values predicted by the method given in reference 15. These values

are for a plate with a laminar boundary layer and were calculated from the following equation:

$$\frac{p_w}{p_\infty} = 1 + \frac{b\bar{x}}{\sqrt{C_w}} + \frac{cI}{2^{2/3}} \quad (3)$$

The magnitude of the viscous boundary-layer growth term $b\bar{x}/\sqrt{C_w}$ was small for these calculations and has little effect on the predictions shown in figures 2(a), (b), (c), and (d). A modification of this equation for the turbulent boundary-layer case is given in appendix B. The calculated pressure distribution for a turbulent boundary layer is essentially the same as for a laminar boundary layer, and therefore is not shown in figure 2. The data in this figure also indicate no difference in pressure distribution between the two types of boundary layers. With a blunt leading edge the boundary-layer profiles showed the trip was an effective means for obtaining a turbulent boundary layer because of the reduced Mach number at the edge of the boundary layer. With a sharp leading edge the use of a trip was not so effective, and transition to a turbulent boundary layer occurred at a considerable distance downstream. The calculated and measured pressure distributions agree reasonably well for the blunted plates, with the exception of the plate with the 0.250-inch leading-edge radius shown in figure 2(a). For this plate a considerable amount of experimental scatter occurred in the data taken on the rear half of the plate.

A
3
6
6

The solid line in figure 2(e) represents values predicted for a laminar boundary-layer growth on a sharp leading-edged flat plate. For this case the data agree fairly well with the predictions based on laminar boundary-layer growth on the forward portion of the plate. Near the end of the plate a slight pressure rise is noted which corresponds to a Mach number gradient of 0.06 per foot and is probably caused by the small Mach number gradient in the test section over this length.

Shock-Wave Shape

The shock-wave shapes for the blunted flat plates were experimentally determined from impact pressure surveys above the surface of the plates. A sudden change in the impact pressure occurred when the probe crossed the shock wave and this determined the location of the shock wave at any particular position along the length of the plate. The dimensionless detachment distance, Δ/d , estimated from measurements compiled in reference 18 was approximately 0.24.

An approximate method was devised in reference 19 by Moeckel to determine the detachment distance and shape of detached shock waves. The method depends only upon body shape and free-stream Mach number. It is based on the following assumptions: (1) that the sonic line is straight out to the shock wave from the point where body slope equals the wedge

angle for shock detachment, and (2) that the shock-wave shape is a hyperbola normal to the free-stream direction on the axis of symmetry and is asymptotic to the free-stream Mach line. The hyperbola is represented by the following equation:

$$Y = \frac{1}{\beta} \sqrt{X^2 - x_0^2} \quad (4)$$

A sketch of the flow field between a blunted flat plate and the shock wave is shown in figure 3(a) and a schematic diagram of the shock wave and the pertinent symbols used in equation (4) are shown in figure 3(b).

Shock-wave shapes as measured on the plate equipped with 0.250-, 0.062-, and 0.015-inch leading-edge radii are shown in figure 4(a). In this figure y_{sw} versus x_{sw} is plotted, where y_{sw} is the ordinate of the shock wave at the distance x_{sw} along the X axis (see insert on fig. 4(a)). The data were obtained when the plate was not equipped with a boundary-layer trip. The boundary layer on the plates, as determined from boundary-layer velocity profiles, was laminar throughout the full length of the plates with 0.250- and 0.062-inch leading-edge radii. For the plate with a 0.015-inch leading-edge radius, the boundary layer was turbulent throughout most of the length. Shock-wave shapes were also experimentally determined for the plates with 0.250- and 0.062-inch leading-edge radii when they were equipped with a boundary-layer trip and the boundary layer was turbulent. These shock-wave shapes did not differ from the ones presented for a laminar boundary layer. The data shown in figure 4(a) are replotted in figure 4(b) as y_{sw}/d versus x_{sw}/d where the shock-wave coordinates are made dimensionless by dividing them by the leading-edge thickness d . A prediction of the shock-wave shape using Moeckel's method (ref. 19) is shown by the solid curve in figure 4(b) labeled $\beta = 4.59$. This value was obtained from the assumption postulated in Moeckel's approximate method that the shape of the shock wave should be a hyperbola asymptotic to the free-stream Mach line. This led to the

value of $\beta = \sqrt{M_\infty^2 - 1}$ in equation (4). As seen from figure 4(b), the data do not agree with the solid curve at the higher values of x_{sw}/d , but do agree reasonably well with the dashed curve labeled $\beta = 3.70$ throughout the entire x_{sw}/d range. Thus, the measured data for the shock-wave shape are correlated with a hyperbola whose asymptote has a slope of 15.1° as shown by the dashed curve in this figure. This angle is considerably higher than the free-stream Mach angle of 12.28° . At large values of x_{sw}/d the slope of this curve is approximately constant and thus is equal to the slope of the asymptote. Therefore the shock-wave shape depicted by the dashed curve appears to represent an outward deflection of the flow over the plate, resulting in a change in the shock-wave angle of approximately 2.82° . The viscous boundary-layer growth term

$b\bar{X}/\sqrt{C_w}$ given in references 7 and 10 predicts that the displacement thickness associated with the boundary-layer growth on these plates results in a shock-wave deflection angle on the order of 0.2° or less,

depending on whether the boundary layer is laminar or turbulent. Therefore, it appears that the increase in shock-wave angle of 2.82° is caused by something other than normal boundary-layer growth.

A theoretical and experimental study of leading-edge bluntness and boundary-layer displacement effects in air at $M = 12.3$ has been reported in reference 20. A considerable portion of the experimental investigation was concerned with the measurement of shock-wave shapes on sharp and blunt leading-edged flat plates. The data from these tests are presented in figure 4(c) where y_{sw} is plotted versus x_{sw} . In figure 4(d) these data are made dimensionless by means of the leading-edge thickness d . Theoretical predictions from the zero order theory and strong blast wave predictions as obtained from reference 20 are also presented in this figure. Curves representing Moeckel's approximate method and its modification identified as $\beta = 12.26$ and $\beta = 5.81$, respectively, are also shown in this figure. Since the data of reference 20 were presented in terms of the horizontal distance from the leading edge of the plate, the dimensionless detachment distance Δ/d was needed for the calculation by Moeckel's method. Measurements obtained from schlieren photographs given in the report served to determine this distance.

From figure 4(d) it can be seen that at large values of x_{sw}/d , Moeckel's approximate method agrees fairly well with the theoretical predictions presented in reference 20. This indicates that all these theoretical predictions assume that the shock wave approaches a Mach line (i.e., $\beta = 12.26$) at large values of x_{sw}/d corresponding to a Mach angle of 4.66° . The data in this figure, however, lie above these predictions, signifying an outward deflection of the flow which is adequately represented by the modified form of Moeckel's method wherein $\beta = 5.81$ which corresponds to an angle of 9.77° .

To investigate in more detail the effect of leading-edge thickness on shock-wave deflection, asymptotes were determined for the shock waves presented in figure 4(c) for $M_\infty = 12.3$ conditions. The angles of the asymptotes are listed as ϕ_{sw} in the table given in figure 4(c). As may be noted from this table, the asymptote angle ϕ_{sw} varies from approximately 7.8° for $d = 0.0002$ inch to 13.2° for $d = 0.203$ inch. These angles are considerably larger than a Mach angle of 4.66° for $M_\infty = 12.3$. Since these shock waves were measured at a constant Mach number and a constant Reynolds number of approximately 74,000 per inch, the increase in shock-wave asymptote angle must be due to an increase in leading-edge thickness. In figure 4(a) insufficient data at higher values of x_{sw} prevented fairing asymptotes through the shock waves for the plate with 0.250- and 0.062-inch leading-edge radii. Therefore, in the present investigation it was not possible to determine the variation in shock-wave asymptote angle with leading-edge radius. The values of β which correlated the shock-wave shapes in figures 4(b) and 4(d) are an average for the different leading-edge thicknesses.

The outward deflection noted in the analysis of these two experimental studies may be due to leading-edge disturbances and/or viscous interaction effects in the flow region between the surface of the plate and the shock wave. Leading-edge disturbances and secondary shock waves, resulting from an overexpansion of the flow around the leading edge, may contribute to maintaining the flow deflection noted in the experimental study. Viscous interaction effects may originate from: (1) boundary-layer growth, and (2) interaction between adjacent layers of fluid moving at different velocities in the shear layer. An analysis of this type concerning the laminar mixing of a compressible fluid is described in reference 21. The possibility of an outward deflection occurring in the flow, when fluids with different velocities mix, can be deduced from this reference. However, additional experimental and theoretical study is needed before positive conclusions can be made.

Static Pressure Gradient Normal to Plate

Static pressures were measured between the plate and the shock wave and are shown in figures 5(a) and (b). As may be noted from these figures, the static pressures near the surface of the plate agree reasonably well with the static pressures measured by the orifices on the plate and remain fairly constant to approximately one-half the distance to the shock wave. At this point the static pressures rise rapidly, and near the shock wave the measured static pressures agree reasonably well with those calculated at the shock wave (see fig. 4(b)). According to calculations for the blunted flat plates at a Mach number of 4.7 which were based on the modified form of Moeckel's method and oblique shock relations in reference 22, the static pressure at the shock wave asymptotically approaches a value of 1.58 times the free-stream static pressure at large distances downstream from the leading edge. Measurements for the other leading-edge configurations showed the same trends with regard to the distribution of the static pressure between the plate surface and the shock wave.

As a result of the agreement between the measured static pressure at the shock wave and the static pressure determined from the shock-wave shape in the current investigation, the static pressure associated with the Mach number 12.3 tests of reference 20 was estimated. The data for this shock-wave shape were previously analyzed and are shown in figures 4(c) and (d). Moeckel's method was used to calculate the values of the static pressure for this shock wave at the same x_{sw}/d values as those for stations 6 and 7 of the model in the present tests. The values were found to be 6.81 and 6.47 times the free-stream static pressure, respectively. The static pressure for this shock wave (i.e., $\beta = 5.81$) was found to approach asymptotically a value of 4.9 times the free-stream static pressure.

Mach Number Distribution in the Shear Layer

Local values of Mach number from the surface of the plate outward to about one-half the distance to the shock wave were determined from the measured impact pressure and surface static pressure. The measured surface static pressure was used to determine the local Mach number because the local static pressure was verified experimentally to be fairly constant in this region, as shown in figure 5. The effect of the actual variation in static pressure on the calculated Mach number distribution is shown in figure 6(a). The ordinate in this figure is the distance y above the plate divided by y_{sw} , the distance between the body surface and the shock wave at the desired station. The Mach number distributions in figure 6(a) were obtained from the data at stations 3 and 11 (see fig. 1) when the boundary layer was laminar on the flat plate with a 0.062-inch leading-edge radius. The solid curves in this figure represent the Mach number distributions determined from the ratio of surface static pressure to the impact pressure above the surface of the plate. The calculations of Mach number distributions shown by the dashed curves were based on a varying static pressure between the plate and the shock wave. The variation in static pressure with distance above the plate was assumed proportional to that determined from the measured distributions shown in figure 5. It can be seen from figure 6(a) that the deviations between the solid and dashed curves are not large in the region from the surface of the plate outward to approximately one-half the distance to the shock wave. Figure 5 further indicates a sharp increase in the static pressure at values greater than one-half the distance to the shock wave. In figure 6(a) deviations resulting from the sharp increase in static pressure in this region can be observed for station 3, as the solid and dashed curves begin to separate. Therefore, the calculation of the Mach number distribution based on a constant surface static pressure appears to be reasonable only up to about one-half the distance to the shock wave.

The Mach number distribution in the vicinity of the shock wave is of particular interest because of the large static pressure gradient in this region. A plot of the Mach number between the edge of the boundary layer and the shock wave obtained from impact pressure surveys measured at station 6 and a static pressure profile assumed to vary in the same proportion as those measured at stations 5 and 7 is shown in figure 6(b). As may be noted from this figure, the Mach number in the shear layer reaches a maximum value at about $y/y_{sw} \approx 0.5$. From there out to the shock wave the Mach number is reduced because of the relatively large static pressure gradient in this region. At the shock wave the low Mach number as shown in figure 6(b) and the high values for static pressure as noted in figure 5 indicate an outward deflection of the flow over the plate. This conclusion is also indicated by the outward deflection of the shock-wave asymptote in figure 4(b).

A
3
6
6

The Mach number distribution in the shear layer for the present tests has been estimated by the method given in reference 23 with a minor static pressure modification. A review of the calculation procedure is given in appendix C. In reference 23 it was assumed that along the plate surface the static pressure equals the free-stream static pressure, p_∞ , and therefore does not vary in the X direction. For blunted plates, this assumption may introduce error since large variations in surface pressures have been found, particularly near the leading edge. In the current investigation, surface static pressure at a particular station or X location was determined by means of equation (3). Therefore, the variation of static pressure along the X direction is the same as shown by the curves in figure 2. The effect of the differences in static pressure at two X locations on the calculated Mach number distribution is shown in figure 7 for a flat plate with a 0.062-inch-radius leading edge. The Mach number distribution is calculated for two widely separated values of x/d on the plate using the surface static pressures. As may be noted from this figure, the difference in the two curves is not large, indicating that the variation in the surface static pressures for the current tests does not have a large effect on the calculated Mach number distribution in the shear layer. The method given in reference 23 also assumes that the static pressure is constant in the region between the surface of the plate and the shock wave at any particular station in the X direction. As indicated in figure 5 this assumption is essentially valid up to approximately one-half the distance to the shock wave. Therefore, the method given in reference 23 might be expected to apply to this region of the flow field.

The local values of Mach number from the surface of the plate outward to about one-half the distance to the shock wave have been determined from data for the flat plates with 0.250-, 0.062- and 0.015-inch leading-edge radii and are shown in figure 8. The data shown in this figure were obtained when the boundary layer was laminar and also when a trip was used to obtain a turbulent boundary layer. It was noticed that weak oblique shock waves were propagated by these boundary-layer trips. However, impact pressure surveys showed that their effect was small and they were neglected. No systematic difference in the Mach number distribution for the two types of boundary layers was found. The Mach number distribution for this region of the flow field has also been calculated by the method of reference 23 using the static pressure modification mentioned earlier. In order to use this method the shock-wave shape must be known; therefore the shock-wave-shape correlation obtained by using $\beta = 3.7$ and $\beta = 4.59$ in equation (4) for the current investigation was used to determine shape of the shock wave as shown in figure 4(b). The Mach number distributions are presented in figure 8 as a means of comparison with the data. Although there is considerable scatter in the measured Mach number distributions, the data from the plate with the 0.250-inch leading-edge radius agree best with the curve labeled $\beta = 4.59$. These data were obtained at small values of x/d which corresponded to the last three stations on the plate where considerable experimental scatter in surface pressures occurred. The data from the plate with the 0.062- and 0.015-inch leading-edge radii agree

with the curve labeled $\beta = 3.7$. There are indications in the data that values of y/Y_{SB} for a particular Mach number, M_1 , increase with the x/d distance along the plate. Data obtained from adjacent stations do not always indicate this trend primarily because of experimental scatter. Such spreading out of the constant Mach number streamlines with distance along the plate is consistent with the flow deflection noted earlier. As the Mach number increases beyond the range of the present tests, the region that would be influenced by the deflection of the flow might extend farther away from the shock wave and cause significant changes near the surface of the plate.

Boundary-Layer Growth

The procedure for calculating boundary-layer growth was similar to one used for predicting turbulent boundary-layer growth in a wind-tunnel nozzle in reference 24. The method is based on the following equation of Von Kármán to evaluate momentum growth:

$$\frac{d\theta}{dx} = \frac{c_f}{2} - \frac{\theta}{M} \frac{dM}{dx} \left(\frac{\frac{\delta^*}{\theta} + 2 - M^2}{1 + \frac{\gamma-1}{2} M^2} \right) \quad (5)$$

Equation (5) was solved in a stepwise manner by inserting local values of the necessary quantities at each point. Small increments of Δx were used and values of θ , M , and c_f were assumed constant over the interval. The Mach number at the end of each interval was determined at the outer edge of the boundary layer. The Mach number distribution normal to the plate was calculated by the method described in appendix C, which is the same method used to calculate the distributions shown in figure 8. The turbulent boundary-layer parameters were determined from references 24 and 25 and were used to obtain the turbulent boundary-layer thickness δ . Local skin-friction coefficients were calculated by the method outlined in reference 24 and also by means of equation (A10) as shown in appendix A. The calculation was started near the leading edge of the plate at a point where local values of Mach number and boundary-layer momentum thickness were determined from a boundary-layer impact pressure survey.

The distribution of the calculated turbulent boundary-layer thickness along the plate is shown in figure 9. Curves are shown for blunted flat plates with 0.062- and 0.015-inch leading-edge radii for the two calculated Mach number distributions in the shear layer which are identified as $\beta = 3.70$ and 4.59 in figures 8(b) and (c). For comparison, a curve of boundary-layer thickness on a sharp leading-edged plate is also shown in figure 9. The boundary-layer thickness does not differ greatly when c_f is calculated by the method given in reference 24 or the T' method (eq. (A10)) as shown by the dashed curves in figure 9(b). As may be noted from this figure the boundary layer on the blunted plates grows at a much faster rate than on the sharp leading-edged plate. The physical

basis for this rapid growth is apparent from equation (5) in which both terms on the right-hand side are additive because M^2 is larger than $\delta^*/\theta + 2$; furthermore dM/dx is large when the boundary-layer edge is in a region of large dM/dy (in the shear layer).

The ratio of the calculated Mach number at the edge of the turbulent boundary layer to the free-stream Mach number is plotted as a function of x/d in figure 10 for the blunted plates with 0.062- and 0.015-inch leading-edge radii. Curves are shown for the two Mach number profiles identified in figures 8(b) and (c) as $\beta = 4.59$ and 3.7. These curves indicate that the boundary layer thickens rapidly when the Mach number at the edge of the boundary layer increases rapidly.

The data shown in figures 9 and 10 for boundary-layer thickness and Mach number at the edge of the boundary layer were evaluated from total pressure surveys in the boundary layer at various stations along the plate. Typical plots of Mach number distributions normal to the plate as determined from these total-pressure surveys are shown in figure 11 for 0.062- and 0.015-inch leading-edge radii. In order to determine the edge of the turbulent boundary layer, the velocity distribution in the boundary layer was assumed to follow a power law. In reference 26 the substitution of a power law was found to correlate turbulent boundary-layer velocity profiles for a sharp flat plate at a free-stream Mach number of 3.0; the velocity profiles measured in the current investigation on the sharp flat plate also were found to correlate with the use of a power law velocity distribution. Therefore, the same method was used for the blunted plates in the current investigation. The velocities and the corresponding y locations in the boundary layer were made dimensionless by means of the velocity corresponding to a y_1 location in the shear layer and then were plotted to a logarithmic scale. Typical plots are shown in figure 11. The departure of the data from a straight line was assumed to be the edge of the boundary layer and, as may be noted from this figure, the edge is not well defined because there is no abrupt deviation from the straight-line plot. In figures 9 and 10 the data for boundary-layer thickness and Mach number at the edge of the boundary layer show the same general trend as the calculated curves, namely a rapid boundary-layer growth in the shear layer.

Heat Transfer

One approach to evaluating turbulent heat-transfer coefficients on blunt leading-edged plates is to use equations for sharp flat plates and modify them to account for local flow conditions. This method has been employed in reference 15 for predicting heat transfer with a laminar boundary layer. Local values of Mach number, temperature, and density at the edge of the boundary layer were used in the calculations. However, the turbulent boundary layer grows at a much faster rate on a

blunted flat plate than on a sharp leading-edged flat plate as shown in figure 9. The turbulent boundary layer also grows at a much faster rate than the laminar boundary layer. Because of this rapid growth, the turbulent boundary layer quickly extends into the large Mach number gradient region. In this region the edge of the boundary layer blends with the shear layer and is difficult to detect by means of an impact-pressure survey. But, in order to evaluate the conditions at the edge of the turbulent boundary layer which determine the heat transfer, it is necessary to predict the turbulent boundary-layer growth.

Comparisons of the measured and predicted heat-transfer rates for the plates with leading-edge configurations of 0.250-, 0.062- and 0.045-inch radii are shown in figure 12. The heat-transfer coefficient, h , versus the distance from the effective start of the turbulent boundary layer, x_t , is plotted in this figure. The data were obtained when the plate was equipped with a boundary-layer trip. The location of the effective start of the turbulent boundary layer was determined by evaluating the boundary-layer momentum thickness near the leading edge of the plate from impact-pressure surveys and then using equation (A8).

The predicted heat-transfer coefficients, represented by the solid curves in figure 12, were obtained by means of equation (A5). In the calculation of these curves, the total pressure at the edge of the boundary layer was assumed to be constant throughout the length of the blunted flat plate and equivalent to that behind the normal shock wave at the nose. The dashed curve in figure 12(b) was calculated from the boundary-layer momentum thickness together with the local flow conditions of Mach number and density at the edge of the boundary layer using equation (A9). (The method for calculating boundary-layer momentum thickness was given in the previous discussion of boundary-layer growth.) As may be noted from figure 12, the data and predictions agree reasonably well. The two methods for predicting heat transfer, as shown by the solid and dashed curves, give results which do not differ appreciably over the length of the blunted flat plates.

A comparison of the heat-transfer coefficients for blunt and sharp leading-edged plates at the same test conditions is shown in figure 13. The ratio of heat-transfer coefficients for plates with blunted leading edges to those calculated for a sharp leading-edged plate is shown in this figure as a function of x_t . The heat-transfer coefficients on the plate with a sharp leading edge were calculated by means of equation (A5). The heat-transfer coefficients predicted for the plates with 0.250- and 0.045-inch leading-edge radii are the same as those given by the solid curves in figures 12(a) and (c). For the plate with a 0.062-inch leading-edge radius, the heat-transfer coefficients were calculated from the boundary-layer momentum thickness in the same manner as that used in evaluating the dashed curve in figure 12(b). As shown in figure 13, the heat-transfer coefficients for the blunted plates do not differ greatly from those calculated for the sharp leading-edged plate. For the plate with a 0.250-inch leading-edge radius, the rates were higher than sharp

plate values only for $x_t < 0.5$. At large values of x_t the coefficients were reduced to approximately 80 percent of sharp-plate values.

At higher Mach numbers the flow field over a blunted plate may be different from that found in this investigation. The basis for this assertion is that at higher Mach numbers the shock wave is closer to the body and the boundary layer is thicker. Therefore, static pressure and other flow parameters at the edge of the boundary layer may be different from those evaluated from surface pressures, and a reduction in turbulent heat transfer for blunted plates compared to sharp leading-edged plates may not occur. This may result from the fact that both turbulent and laminar heat-transfer coefficients increase with increasing density or pressure at the edge of the boundary layer.

SUMMARY OF RESULTS

The following conclusions are made from measurements of the flow field and the turbulent heat-transfer coefficient over blunted flat plates at a Mach number of 4.7:

1. Measurements of the shock-wave shape and static pressure surveys indicated an outward deflection of the shock-wave asymptote of approximately 2.82° . Flow deflection due to boundary-layer growth was estimated to account for a shock-wave deflection of only 0.2° . Therefore, other phenomena associated with the flow field must contribute to the observed shock wave deflection.
2. Mach number distributions measured in the shear layer agreed with predictions (based on measured shock-wave shapes) at downstream locations on the plate that are greater than 40 leading-edge diameters. At stations closer to the leading edge the agreement was not so good.
3. Measured and calculated turbulent boundary-layer growth is rapid when the outer edge of the boundary layer is in a large Mach number gradient region.
4. Predictions of turbulent heat-transfer coefficients for blunted plates were in agreement with measured heat-transfer coefficients. A comparison between blunt and sharp leading-edged plates indicated that the heat-transfer coefficients near the leading edge (back to 10 leading-edge diameters) were higher for the blunted plates and decreased to approximately 80 percent of the sharp-plate values at a considerable distance from the leading edge.

APPENDIX A

CALCULATIONS OF THE EFFECTIVE ORIGIN OF THE TURBULENT BOUNDARY LAYER
AND STANTON NUMBER, AND SKIN-FRICTION COEFFICIENT
AS A FUNCTION OF THE MOMENTUM THICKNESS

Colburn's modification of Reynolds analogy gives the local skin-friction coefficient as:

$$\frac{c_f}{2} = St(Pr)^{2/3} \quad (A1)$$

but it can also be stated in terms of the rate of growth of the momentum thickness

$$\frac{c_f}{2} = \frac{d\theta}{dx_t} \quad (A2)$$

and if no temperature or pressure gradient is assumed,

$$\frac{d\theta}{dx_t} = \frac{dR_\theta}{dR_x} \quad (A3)$$

if R_x is based on an effective leading-edge distance. Thus,

$$\frac{dR_\theta}{dR_x} = St(Pr)^{2/3} \quad (A4)$$

In reference 27, it was found that if $(Pr)^{2/3}$ is set equal to $1/1.2$, the Reynolds analogy holds over a wide range of Reynolds numbers. This substitution is combined with the approximation to the Kármán-Schoenherr equation in the same manner as given in reference 16:

$$St = \frac{0.026}{R_x^{0.18} \left(\frac{T'}{T_e} \right)^n} \quad (A5)$$

to form

$$\frac{c_f}{2} = \frac{dR_\theta}{dR_x} = \frac{0.0217}{R_x^{0.18} \left(\frac{T'}{T_e} \right)^n} \quad (A6)$$

Integrating equation (A6) and transposing

$$R_x = 84.0 R_\theta^{1.22} \left(\frac{T'}{T_e} \right)^{1.22n} \quad (A7)$$

which can be solved for the distance from an effective leading edge

$$x_t = 84.0 R_\theta^{1.22} \left(\frac{T'}{T_e} \right)^{1.22n} \frac{\mu_e}{\rho_e u_e} \quad (A8)$$

The value of the exponent n is dependent on the exponent in the power law relationship between temperature and viscosity. For the temperature conditions which prevailed during these tests, values of n were chosen as 0.67 and 0.65 for the plates with blunted and sharp leading edges, respectively.

If equation (A7) is substituted in equation (A5), there results an equation for St based on R_θ . For $n = 0.67$, this equation is

$$St = \frac{0.0117}{R_\theta^{0.22} \left(\frac{T'}{T_e} \right)^{0.82}} \quad (A9)$$

By means of the Reynolds analogy, the local skin-friction coefficient can be determined from equation (A9) as follows:

$$c_f = \frac{0.0195}{R_\theta^{0.22} \left(\frac{T'}{T_e} \right)^{0.82}} \quad (A10)$$

A
3
6
6

APPENDIX B

PRESSURE DISTRIBUTION ON SURFACE WITH A TURBULENT BOUNDARY LAYER

The determination of the pressure distribution in the current investigation is based on the method employed in reference 15 for predicting the pressure distribution along the surface of a plate with a laminar boundary layer. The procedure used in reference 15 is based on the following equation:

$$\frac{p_w}{p_\infty} = 1 + \gamma M_e \frac{d\delta^*}{dx} + \frac{cI}{2^{2/3}} \quad (B1)$$

where M_e is the reduced total head Mach number obtained from normal shock relations. The following relation is valid for a laminar boundary layer along the surface of the plate:

$$\gamma M_e \frac{d\delta^*}{dx} = \frac{b\bar{x}}{\sqrt{C_w}} \quad (B2)$$

and the terms in equation (B2) are defined as:

$$b = \left[\frac{0.865}{M_e^2} \frac{T_w}{T_\infty} + 0.166(\gamma - 1) \right] \gamma \quad (B3)$$

$$\bar{x} = \frac{M_e^3 \sqrt{C_w}}{\sqrt{R_x}} \quad (B4)$$

$$C_w = \frac{\mu_w T_e}{\mu_e T_w} \quad (B5)$$

For air, $c = 0.112 (C_D)^{2/3}$ and for a cylinder,

$$C_D = 0.112 \quad (B6)$$

According to inviscid-flow theory, the term $b\bar{x}/\sqrt{C_w}$ in equation (B2) accounts for the laminar boundary-layer displacement growth, and to determine surface-pressure distribution, the expression for the effective shape of the body should include this term for boundary-layer growth.

In order to evaluate the displacement thickness growth of the turbulent boundary layer, the following procedure is used:

From equation (A6)

$$\frac{C_f}{2} = \frac{1}{x} \int_0^x \frac{0.0217 \, dx}{R_x^{0.18} \left(\frac{T'}{T_e} \right)^{0.67}} \quad (B7)$$

Integrating (B7)

$$\frac{C_f}{2} = \frac{0.0264}{R_x^{0.18} \left(\frac{T'}{T_e} \right)^{0.67}} \quad (B8)$$

Now

$$\theta = \frac{C_f}{2} x = \frac{0.0264 \, x}{R_x^{0.18} \left(\frac{T'}{T_e} \right)^{0.67}} \quad (B9)$$

and

$$\delta^* = \theta \frac{\delta^*}{\theta} = \frac{0.0264 \, x}{R_x^{0.18} \left(\frac{T'}{T_e} \right)^{0.67}} H \quad (B10)$$

Differentiating equation (B10), we obtain:

$$\frac{d\delta^*}{dx} = \frac{0.0217}{R_x^{0.18} \left(\frac{T'}{T_e} \right)^{0.67}} H \quad (B11)$$

which when substituted in equation (B1) gives the general expression for the pressure ratio for the turbulent boundary layer along the surface of the plate; if x , the distance from the leading edge of the plate, is assumed equal to x_t , the distance from the turbulent boundary-layer origin. Thus,

$$\frac{p_w}{p_\infty} = 1 + \frac{0.0217}{R_x^{0.18} \left(\frac{T'}{T_e} \right)^{0.67}} H(\gamma M_e) + \frac{cI}{2^{2/3}} \quad (B12)$$

APPENDIX C

MOECKEL'S METHOD FOR CALCULATING MACH NUMBER PROFILES

IN THE SHEAR LAYER FOR DETACHED SHOCK WAVES

The analysis and equations given in this appendix are essentially the same as those in references 19 and 23. They are repeated here in order to define the symbols and to follow more easily the discussion of the flow field analyzed in this paper.

The continuity equation (see fig. 3) can be written across the shock wave with the sonic-point area used for reference as follows:

$$\frac{a}{A_{SB}} = \int_0^{A/A_{SB}} \frac{\rho_{\infty} u_{\infty}}{\rho u} d \left(\frac{A}{A_{SB}} \right) \quad (C1)$$

or

$$\frac{a}{A_{SB}} = \int_0^{A/A_{SB}} \frac{P_{\infty} (A^*/A)_{M_{\infty}}}{P (A^*/A)_M} d \left(\frac{A}{A_{SB}} \right) \quad (C2)$$

Since it is assumed that the stagnation pressure remains constant along a streamline downstream of the shock wave, P/P_{∞} is the stagnation-pressure ratio across the shock at the point where the streamline defining the area A enters the shock. If the shock angle at this point is ϕ , then according to reference 22 the total pressure ratio can be written

$$\frac{P}{P_{\infty}} = \left(\frac{6M_{\infty}^2 \sin^2 \phi}{M_{\infty}^2 \sin^2 \phi + 5} \right)^{\gamma/(\gamma-1)} \left(\frac{6}{7M_{\infty}^2 \sin^2 \phi - 1} \right)^{1/(\gamma-1)} \quad (C3)$$

The Mach number M , at the area a , can also be related to the shock angle by the relation

$$1 + 0.2M^2 = \left(\frac{P}{P_{\infty}} \right)^{(\gamma-1)/\gamma} = \left(\frac{P}{P_{\infty}} \frac{P_{\infty}}{P_{\infty}} \frac{P_{\infty}}{P} \right)^{(\gamma-1)/\gamma} \quad (C4)$$

By means of equation (C4) and other identities in reference 22 equation (C2) can be expressed as follows:

$$\frac{a}{A_{SB}} = \int_0^{A/A_{SB}} \frac{M_{\infty}}{M} \frac{P_{\infty}}{P} \left(\frac{1 + 0.2M_{\infty}^2}{1 + 0.2M^2} \right)^{1/2} d \left(\frac{A}{A_{SB}} \right) \quad (C5)$$

By means of equations (C3) and (C4), M in equation (C5) can be related to the angle at the point where the streamline crosses the shock wave. The differential $d(A/A_{SB})$ must be converted into a function in order that the integration may be carried out from $\varphi = 90^\circ$ to $\varphi = \varphi_1$, where φ_1 is the upper limit of integration.

From reference 19, if the shock-wave shape is assumed to be a hyperbola, the equation of the shock wave in the notation given in figure 3 is:

$$Y = \frac{1}{\beta} \sqrt{X^2 - x_o^2} \quad (C6)$$

where $1/\beta$ is the slope of the asymptote. Then

$$\frac{dY}{dX} = \tan \varphi = \frac{X}{\beta \sqrt{X^2 - x_o^2}} = \frac{\sqrt{x_o^2 + \beta^2 Y^2}}{\beta^2 Y^2} \quad (C7)$$

and by algebraic manipulation

$$Y^2 = \frac{x_o^2}{\beta^2(\beta^2 \tan^2 \varphi - 1)} \quad (C8)$$

If Y_{SB} is the reference location on the body, equation (C8) can be expressed as

$$\left(\frac{Y}{Y_{SB}}\right)^2 = \frac{(x_o/Y_{SB})^2}{\beta^2(\beta^2 \tan^2 \varphi - 1)} \quad (C9)$$

where

$$\frac{x_o}{Y_{SB}} = \beta \frac{Y_s}{Y_{SB}} \sqrt{\beta^2 \tan^2 \varphi_s - 1} \quad (C10)$$

The differential $d(A/A_{SB})$ is determined from equation (C9) as,

$$d\left(\frac{A}{A_{SB}}\right) = d\left(\frac{Y}{Y_{SB}}\right) = -\beta \frac{x_o}{Y_{SB}} \left[\frac{\tan \varphi \sec^2 \varphi d\varphi}{(\beta^2 \tan^2 \varphi - 1)^{3/2}} \right] \quad (C11)$$

Substituting equations (C10) and (C11) into equation (C5),

$$\frac{a}{A_{SB}} = \frac{y}{Y_{SB}} = -\beta^2 \frac{Y_S}{Y_{SB}} \sqrt{\beta^2 \tan^2 \varphi_S - 1} \int_{\varphi_0}^{\varphi_1} \frac{P_\infty}{P} \left(\frac{1 + 0.2 M_\infty^2}{1 + 0.2 M^2} \right)^{1/2} \frac{M_\infty}{M} \left[\frac{\tan \varphi \sec^2 \varphi}{(\beta^2 \tan^2 \varphi - 1)^{3/2}} \right] d\varphi \quad (C12)$$

The value of Y_S/Y_{SB} depends upon the location of the sonic line and is given in reference 19 as follows:

$$\frac{Y_S}{Y_{SB}} = \frac{1}{(1 - B \cos \eta)} \quad (C13)$$

where

$$\eta \cong \lambda_d \cong \lambda_S \quad (C14)$$

and

$$B = \left(\frac{A^*}{A} \right)_{M_\infty} \left(\frac{P_\infty}{P_S} \right)_c \quad (C15)$$

The ratio $(P_\infty/P_S)_c$ is determined from equation (C3) with φ equal to φ_c as follows:

$$\varphi_c = \tan^{-1} \frac{1}{\beta} (4\beta^2 \tan^2 \varphi_S - 3)^{1/2} \quad (C16)$$

The Mach number profiles above the plate were determined from equation (C12). In reference 23 the static pressure, p , in equation (C12) was assumed to be equal to that in the undisturbed free stream. As may be noted from figure 2, however, the static pressure varies considerably from free-stream values and depends upon the leading-edge bluntness and the value of x . Therefore, when computing the Mach number profiles, the static pressure at a particular x value was assumed to correspond to values determined from the calculated curves shown in figure 2 which agree reasonably well with measured values.

When methods were evaluated to predict shock-wave shapes, the method given in reference 28 was also considered. However, it was found that the shock-wave shape as predicted by either reference 19 or 28 did not differ appreciably for the conditions in this investigation. This may not be true for three-dimensional bodies since the method of reference 28 is concerned primarily with shock-wave shapes in the vicinity of the nose. It is interesting to note that the equation to predict shock-wave shape is practically the same for the two methods and the difference is essentially in evaluating the slope, η , of the sonic line. In reference 28 this slope is evaluated from a correlation of measured shock-wave shapes; whereas in reference 19 the slope is determined from an average of the flow directions at the surface of the body and at the shock wave, assuming a straight sonic line.

REFERENCES

1. Becker, J. V.: Results in Recent Hypersonic and Unsteady Flow Research at the Langley Aeronautical Laboratory. Jour. Appl. Phys., vol. 21, no. 7, July 1950, pp. 622-624.
2. Shen, S. F.: An Estimate of Viscosity Effect in Hypersonic Flow Over an Insulated Wedge. Jour. Math. and Phys., vol. 31, no. 3, Oct. 1952, pp. 192-205.
3. Li, Ting-Yi, and Nagamatsu, H.: Shock Wave Effects on the Laminar Skin Friction of an Insulated Flat Plate at Hypersonic Speeds. Jour. Aero. Sci., vol. 20, no. 5, May 1953, pp. 345-355.
4. Pai, Shih-I.: On Strong Interaction for the Hypersonic Boundary Layers on an Inclined Wedge. Jour. Aero. Sci., vol. 20, no. 11, Nov. 1953, p. 796.
5. Li, Ting-Yi, and Nagamatsu, H. T.: Hypersonic Viscous Flow on a Non-insulated Flat Plate. GALCIT no. 25, April 1955.
6. Bertram, Mitchel H.: An Approximate Method for Determining the Displacement Effects and Viscous Drag of Laminar Boundary Layers in Two-Dimensional Hypersonic Flow. NACA TN 2773, 1952.
7. Lees, Lester, and Probst, Ronald F.: Hypersonic Viscous Flow Over a Flat Plate. Princeton Univ. Aero. Eng. Lab. Rep. 195, April 20, 1952.
8. Lees, Lester: On the Boundary Layer Equations in Hypersonic Flow and Their Approximate Solutions. Princeton Univ. Aero. Eng. Lab. Rep. 212, Sept. 1952.
9. Lees, Lester: Influence of the Leading Edge Shock Wave on the Laminar Boundary Layer at Hypersonic Speeds. Jour. Aero Sci., vol. 23, no. 6, June 1956, pp. 594-600.
10. Hammitt, Andrew G.: The Hypersonic Viscous Effect on a Flat Plate with Finite Leading Edge. Princeton Univ. Aero. Eng. Lab. Rep. 378, Mar. 1957.
11. Hammitt, A. G., Vas, I. E., and Bogdonoff, S. M.: Leading Edge Effects on the Flow Over a Flat Plate at Hypersonic Speeds. Princeton Univ. Aero. Eng. Rep. 326, Sept. 1955.
12. Lees, Lester: Inviscid Hypersonic Flow Over Blunt-Nosed Slender Bodies. GALCIT Memo 31, Feb. 1, 1956.

13. Lees, Lester, and Kubota, Toshi: Inviscid Hypersonic Flow Over Blunt-Nosed Slender Bodies. Jour. Aero. Sci., vol. 24, no. 3, Mar. 1957, pp. 195-202.
14. Cheng, H. K., and Pallone, A. S.: Inviscid Leading-Edge Effect in Hypersonic Flow. Jour. Aero. Sci., vol. 23, no. 7, July 1956, pp. 700-702.
15. Creager, Marcus O.: Effects of Leading-Edge Blunting On the Local Heat Transfer and Pressure Distributions Over Flat Plates In Supersonic Flow. NACA TN 4142, 1957.
16. Tendeland, Thorval: Effects of Mach Number and Wall-Temperature Ratio on Turbulent Heat Transfer at Mach Number From 3 to 5. NASA TR R-16, 1959. A
3
6
6
17. Douglas, Thomas B., and Dever, James L.: Enthalpy and Specific Heat of Four Corrosion-Resistant Alloys at High Temperatures. Jour. of the National Bureau of Standards, vol. 54, no. 1, Jan. 1955, pp. 15-19. (Also NBS Res. Paper 2560)
18. Liepmann, H. W., and Roshko, A.: Elements of Gasdynamics. GALCIT Aeronautical Series, John Wiley and Sons, Inc., March 1958, p. 105.
19. Moeckel, W. E.: Approximate Method for Predicting Form and Location of Detached Shock Waves Ahead of Plate or Axially-Symmetric Bodies. NACA TN 1921, 1949.
20. Cheng, H. K., Hall, J. Gordon, Golian, T. C., and Hertzberg, A.: Boundary-Layer Displacement and Leading-Edge Bluntness Effects in High-Temperature Hypersonic Flow. IAS Paper no. 60-38, Jan. 1960.
21. Chapman, Dean R.: Laminar Mixing of a Compressible Fluid. NACA TN 1800, 1949.
22. Ames Research Staff: Equation, Tables, and Charts for Compressible Flow. NACA Rep. 1135, 1953.
23. Moeckel, W. E.: Some Effects of Bluntness on Boundary-Layer Transition and Heat Transfer at Supersonic Speeds. NACA TR 1312, 1957.
24. Persh, Jerome, and Lee, Roland: A Method of Calculating Turbulent Boundary Layer Development in Supersonic and Hypersonic Nozzles Including the Effects of Heat Transfer. NavOrd Rep. 4200, U. S. Naval Ord. Lab., June 1956.
25. Persh, Jerome, and Lee, Roland: Tabulation of Compressible Turbulent Boundary Layer Parameters. NavOrd Rep. 4282, U. S. Naval Ord. Lab., May 1956.

26. Nothwang, George J.: An Evaluation of Four Experimental Methods for Measuring Mean Properties of a Supersonic Turbulent Boundary Layer. NACA TR 1320, 1957.
27. Rubesin, Morris W.: A Modified Reynolds Analogy for the Compressible Turbulent Boundary Layer on a Flat Plate. NACA TN 2917, 1953.
28. Love, Eugene S.: A Re-examination of the Use of Simple Concepts for Predicting the Shape and Location of Detached Shock Waves. NACA TN 4170, 1957.

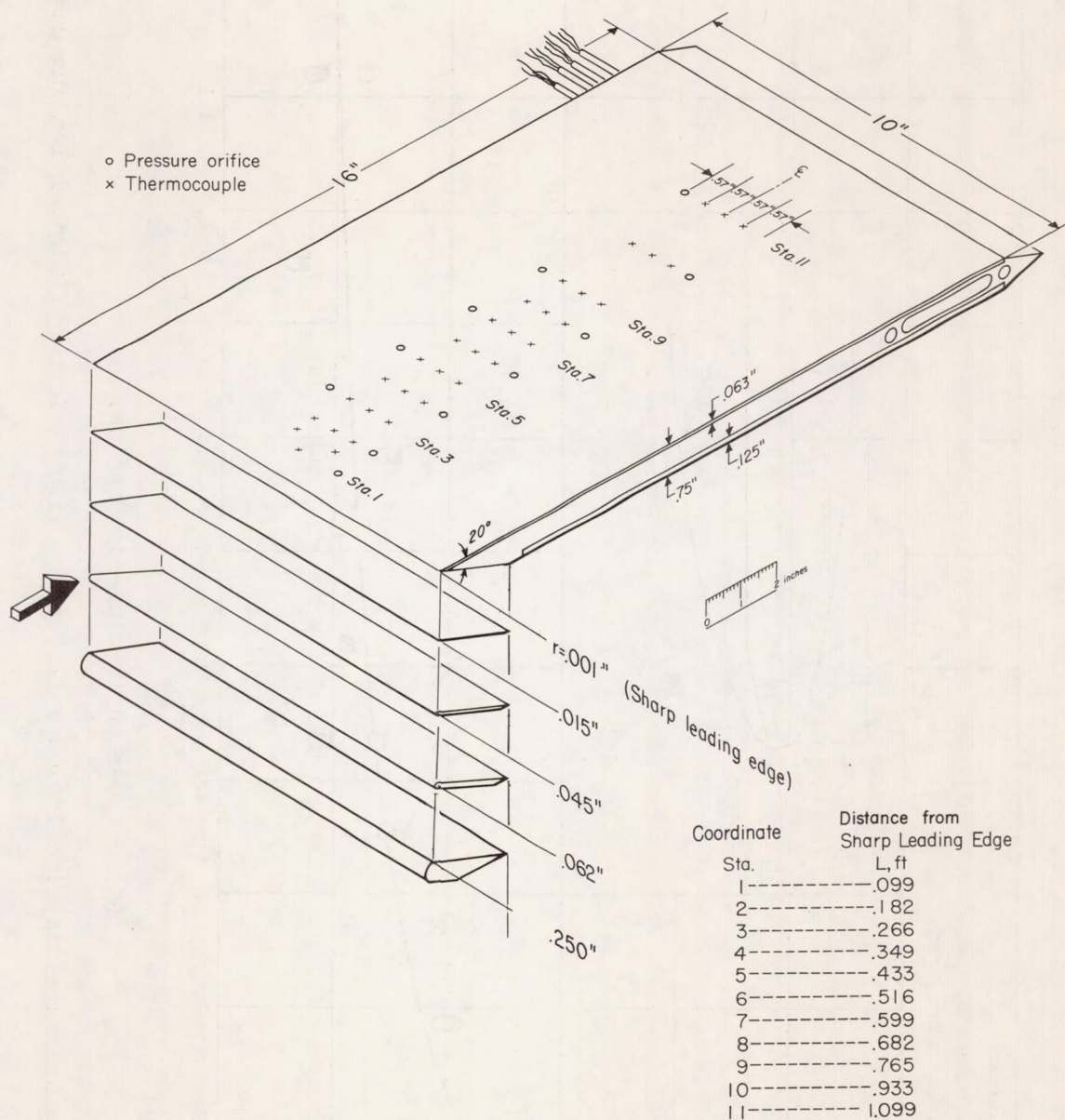
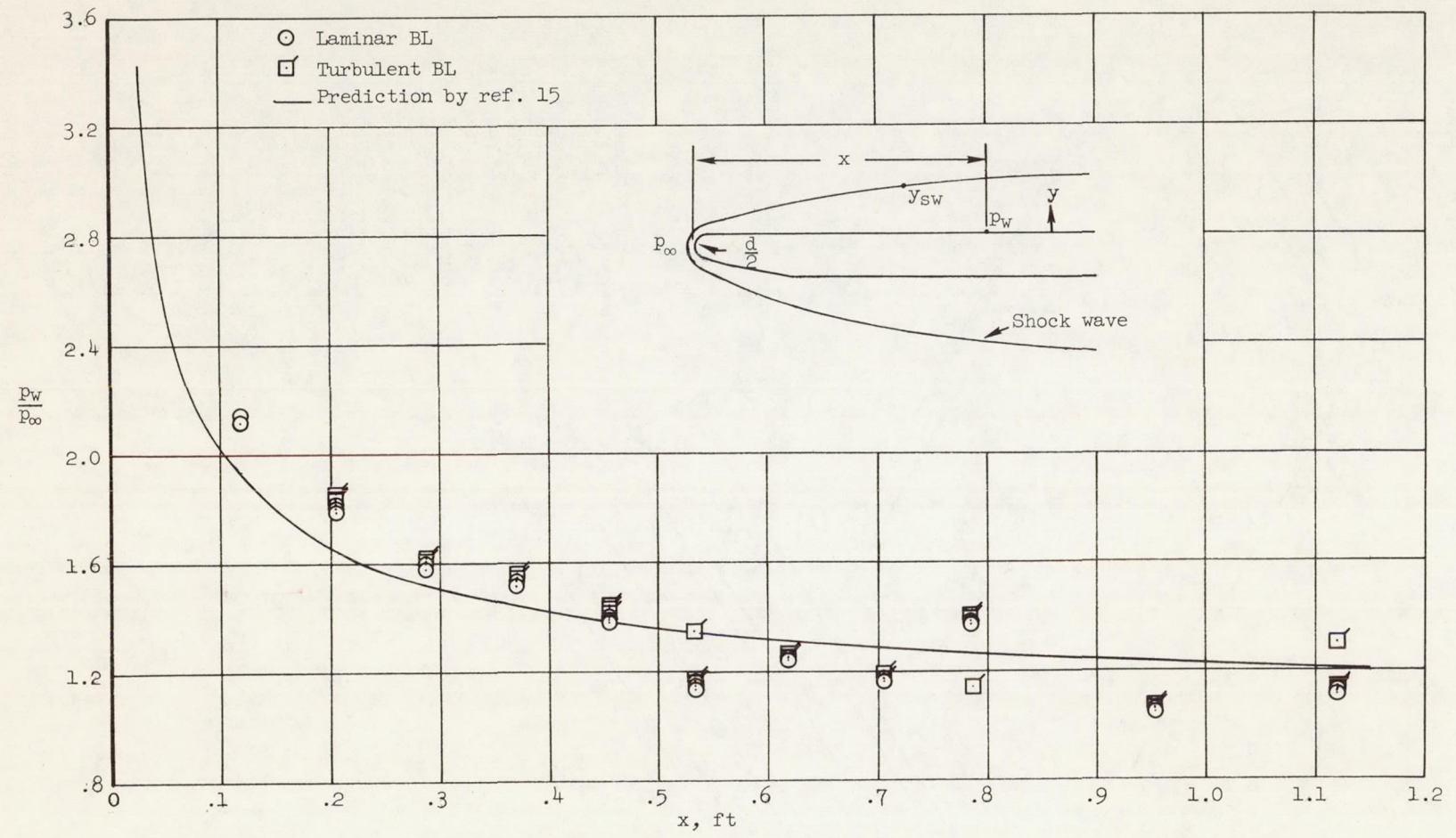
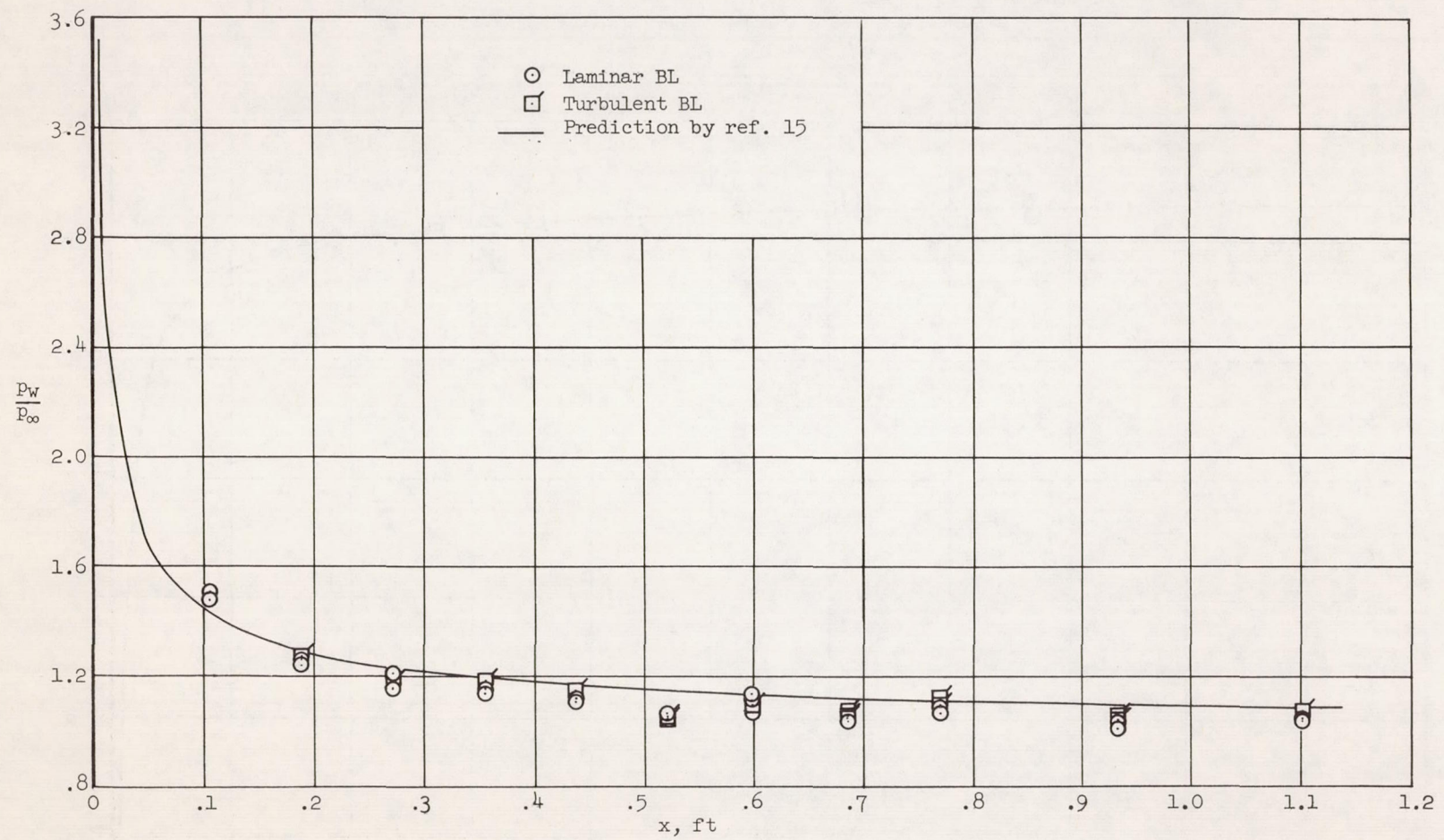


Figure 1.- Sketch of test body.



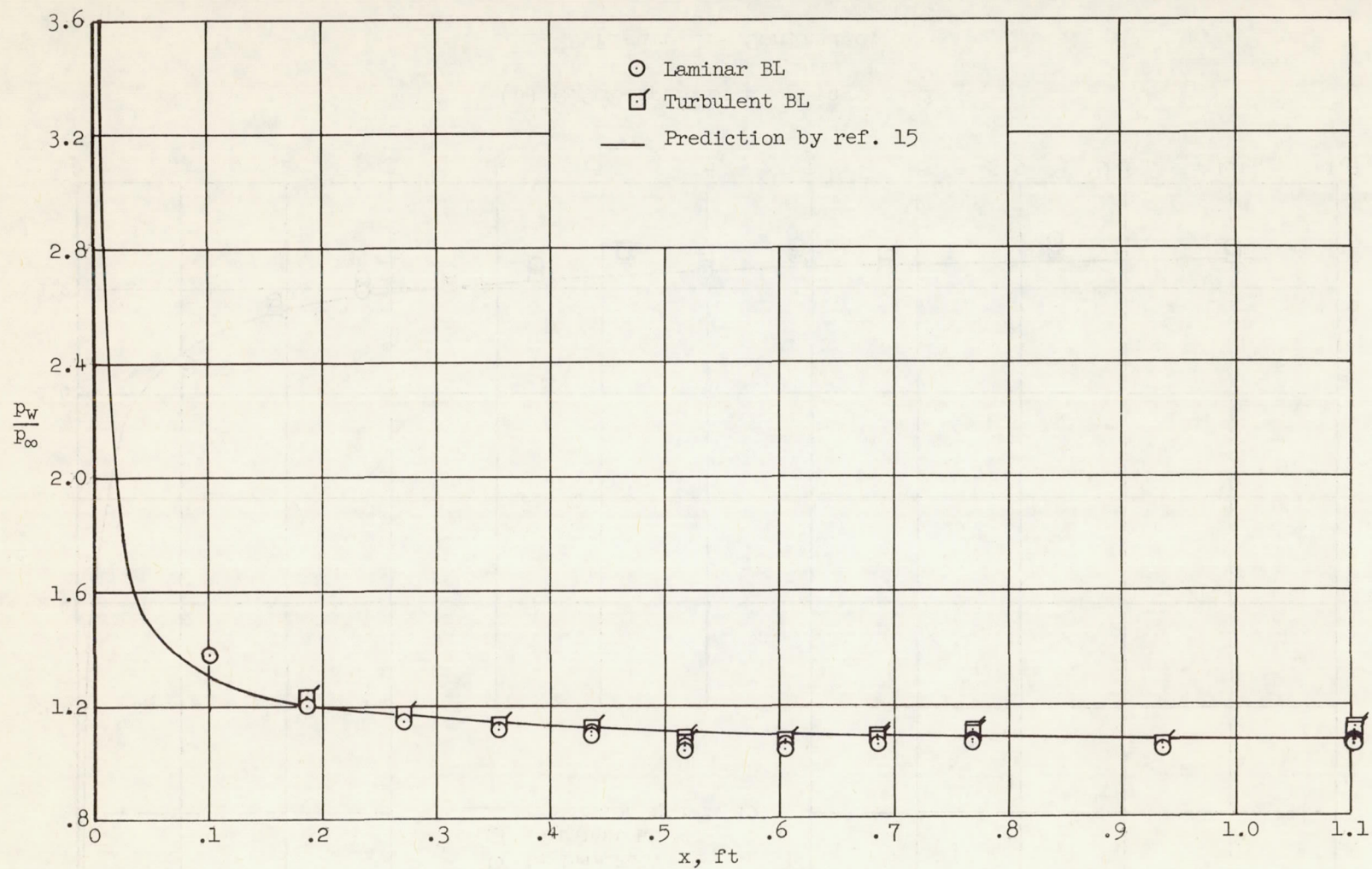
(a) 0.250-inch leading-edge radius.

Figure 2.- Surface pressure distribution on a flat plate with various cylindrical leading edges.



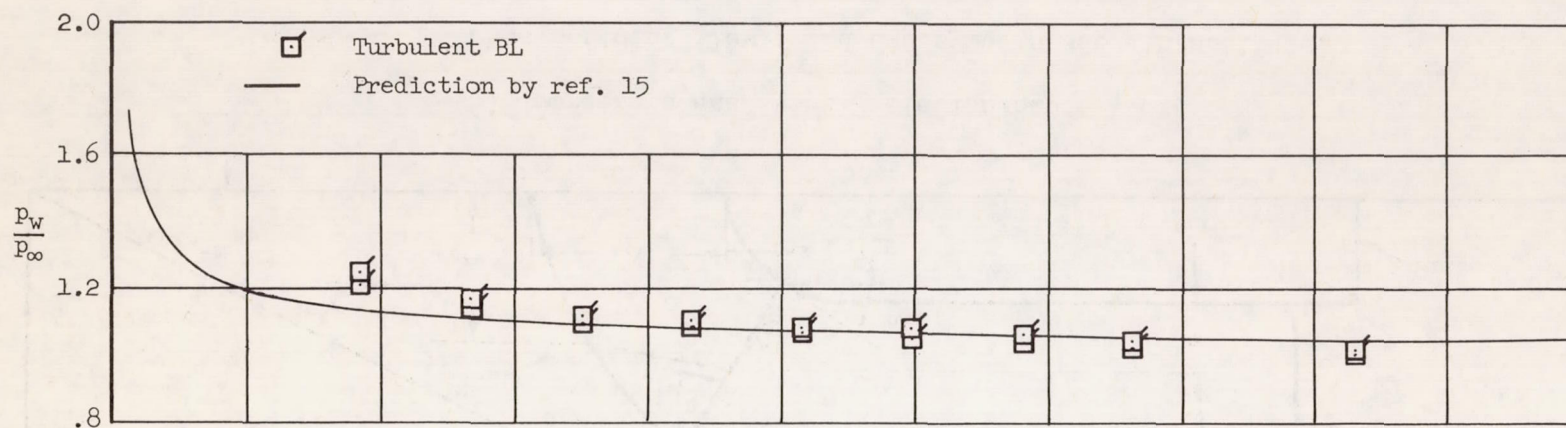
(b) 0.062-inch leading-edge radius.

Figure 2.- Continued.

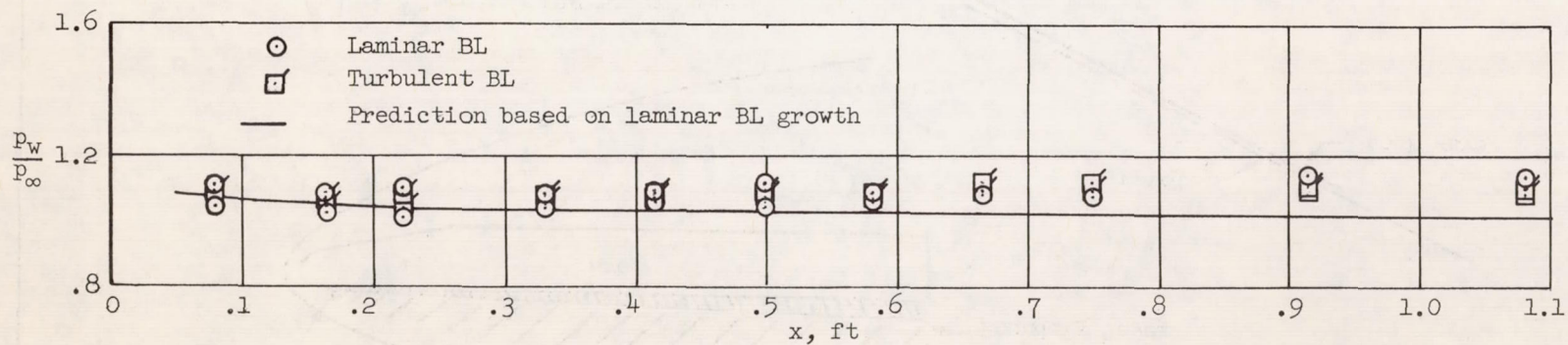


(c) 0.045-inch leading-edge radius.

Figure 2.- Continued.



(d) 0.015-inch leading-edge radius.



(e) Sharp leading-edged plate.

Figure 2.- Concluded.

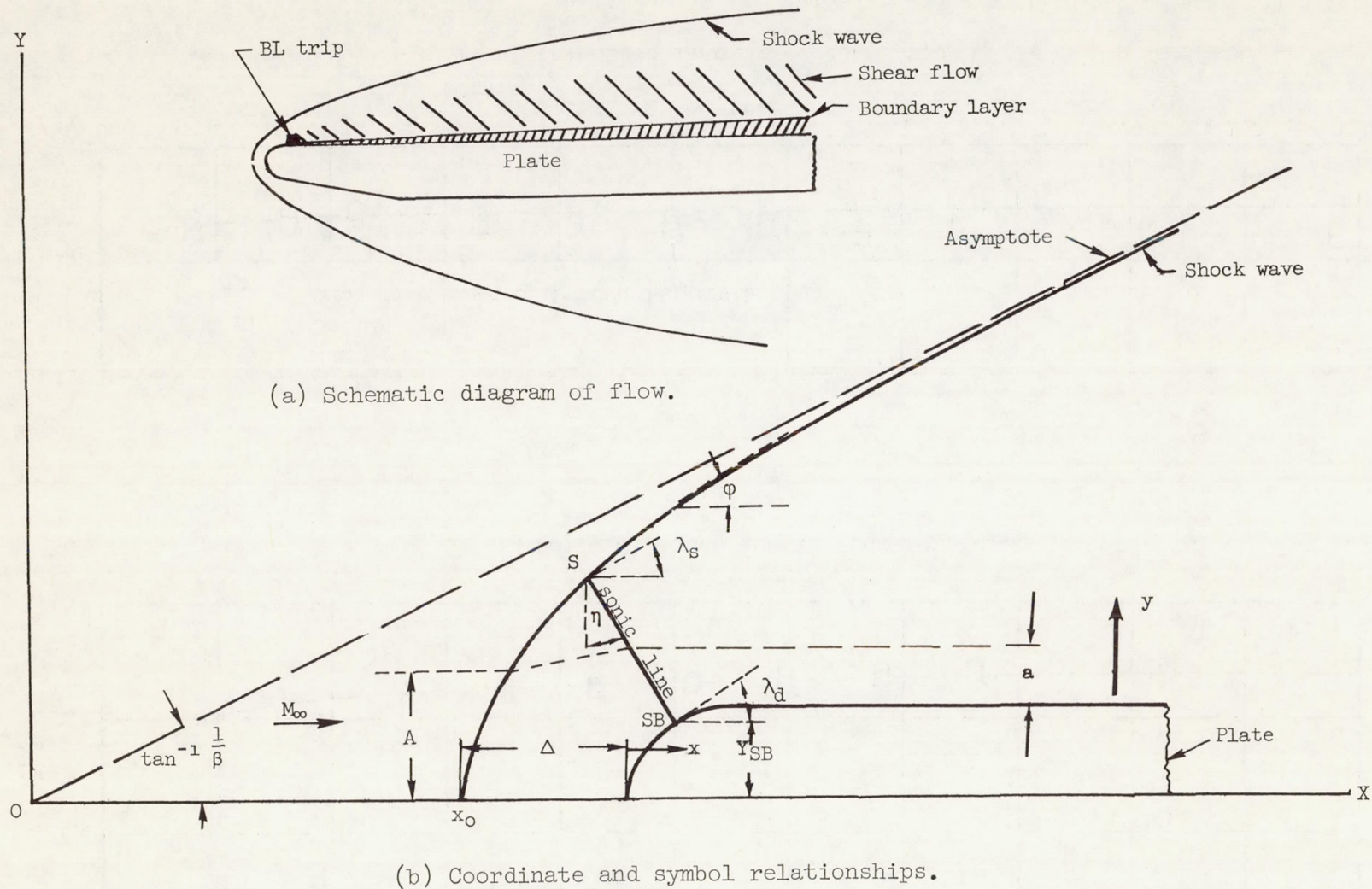
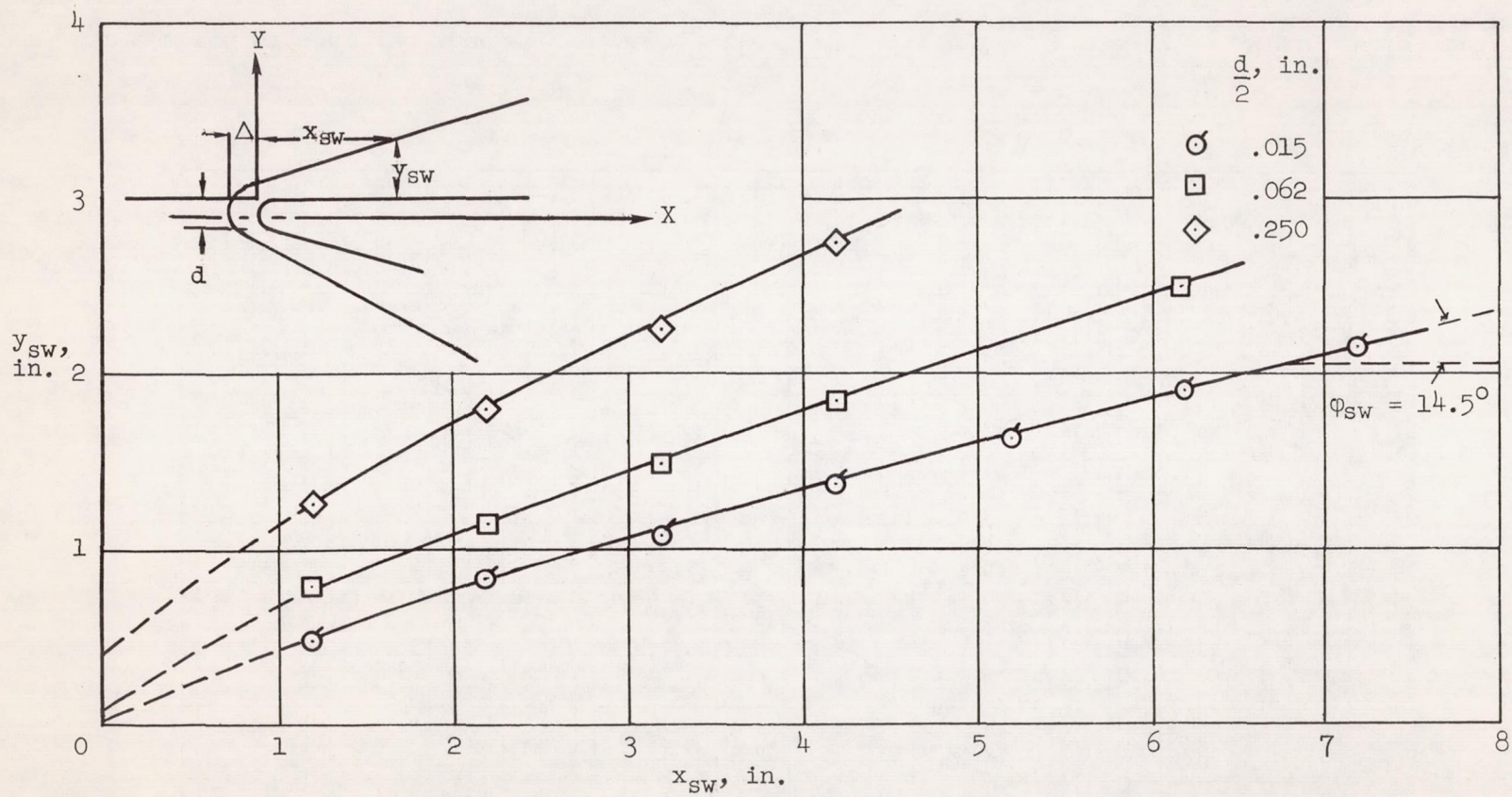
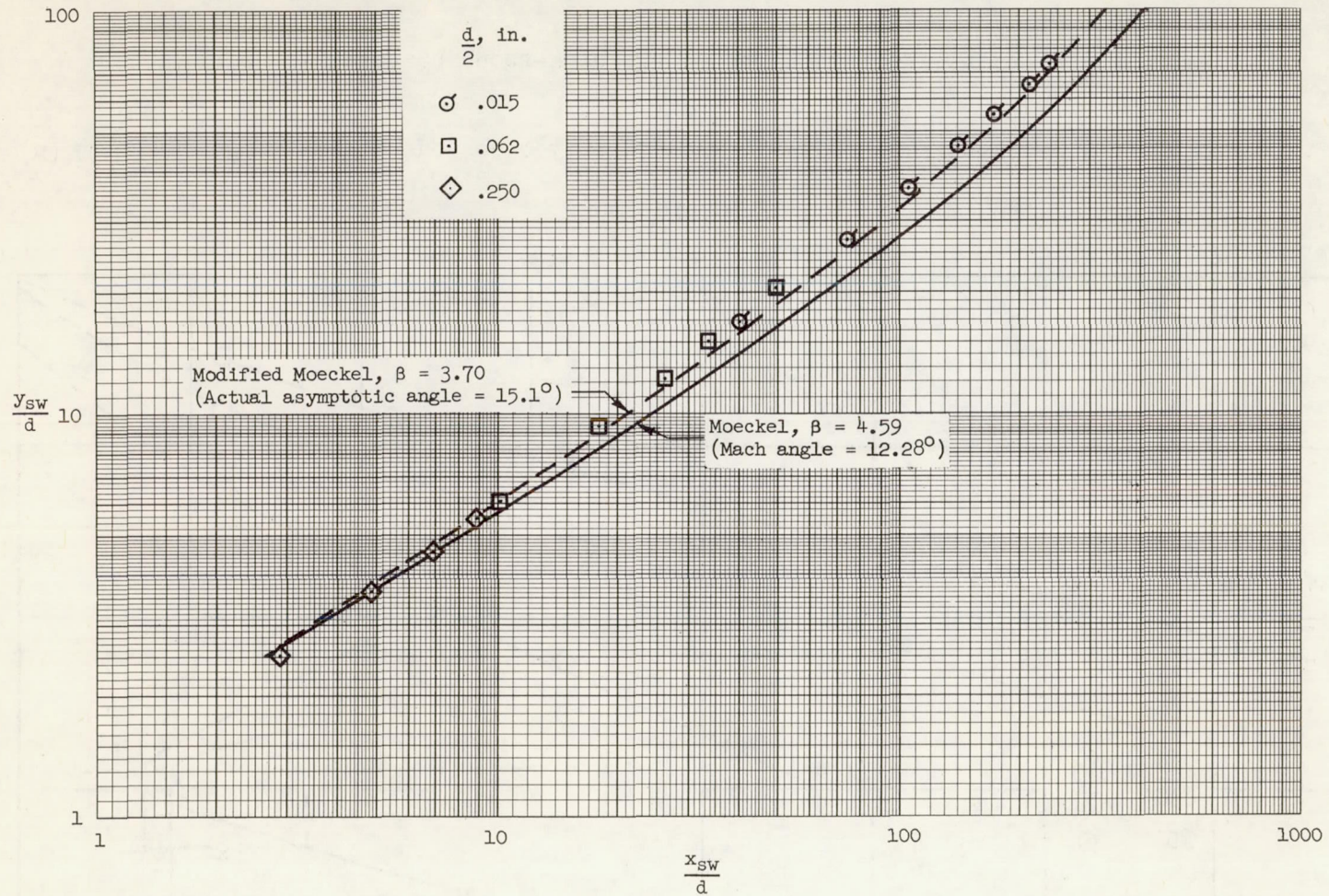


Figure 3.- Sketches defining flow field and symbols used in analysis.



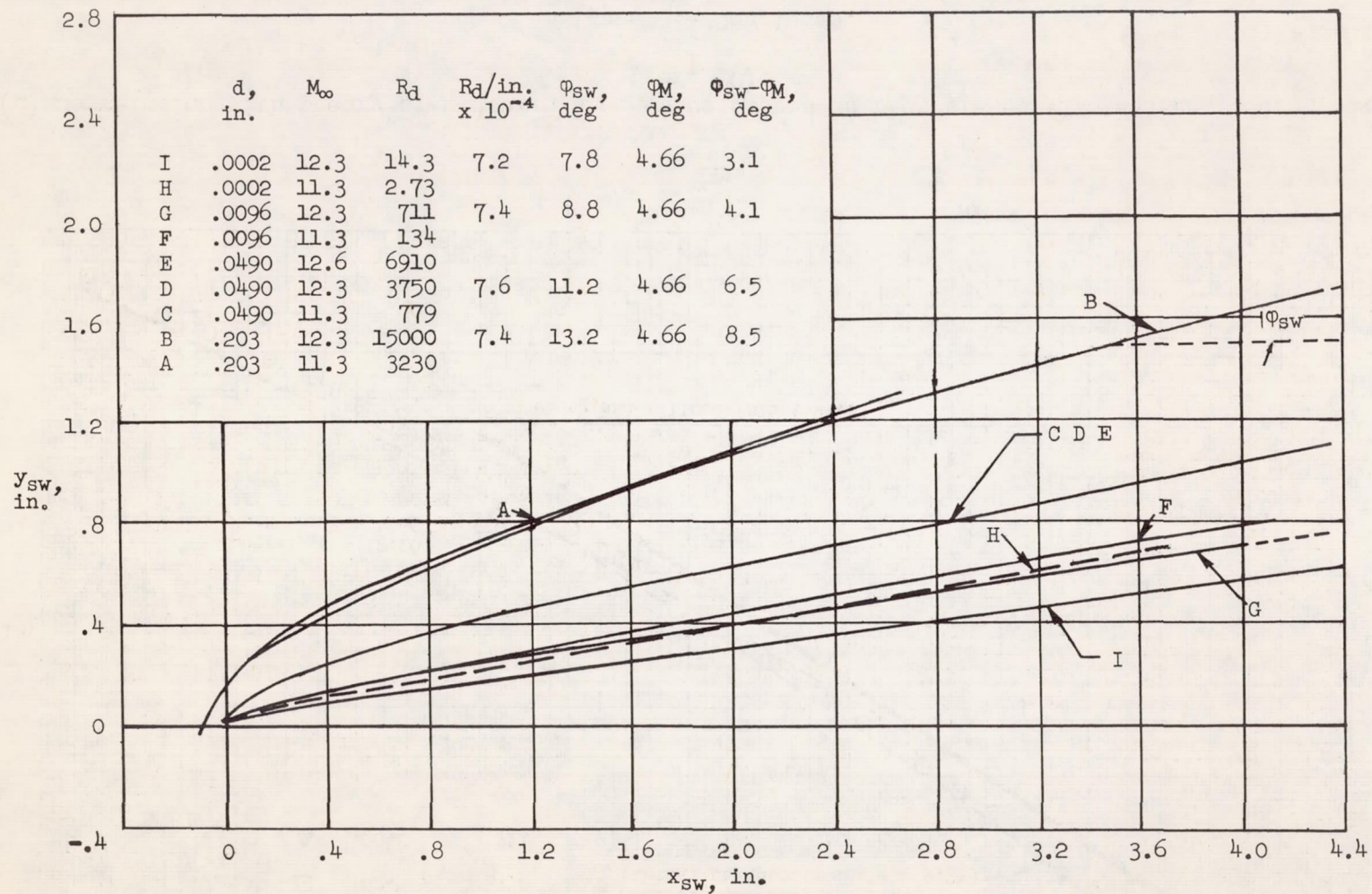
(a) Measured shock-wave shapes on a flat plate with various cylindrical leading edges in air at $M_\infty = 4.7$.

Figure 4.- Measured shock-wave shapes and their correlation with theory.



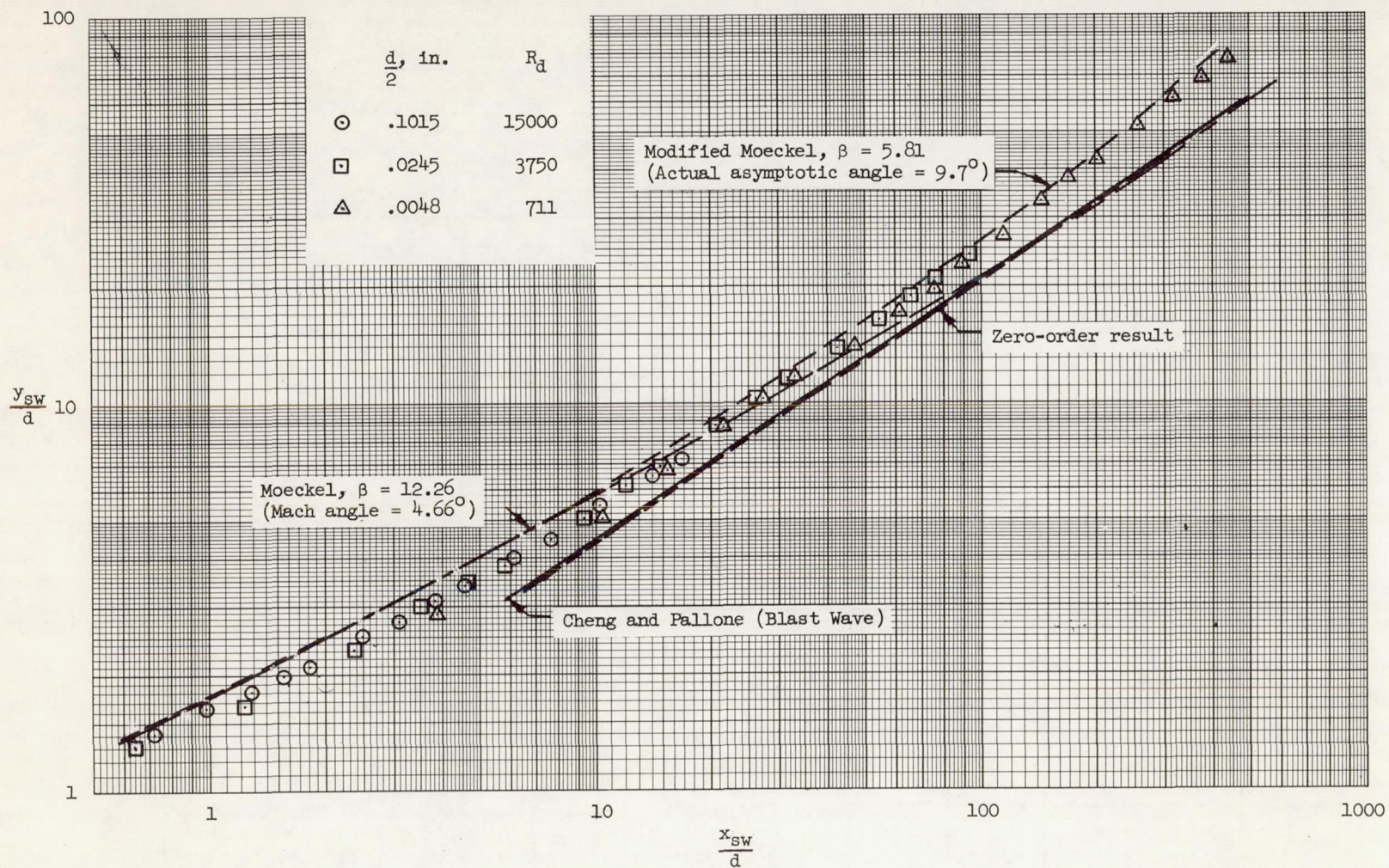
(b) Correlation of measured shock-wave shapes with theory for a flat plate with various cylindrical leading edges in air at $M_\infty = 4.7$.

Figure 4.- Continued.



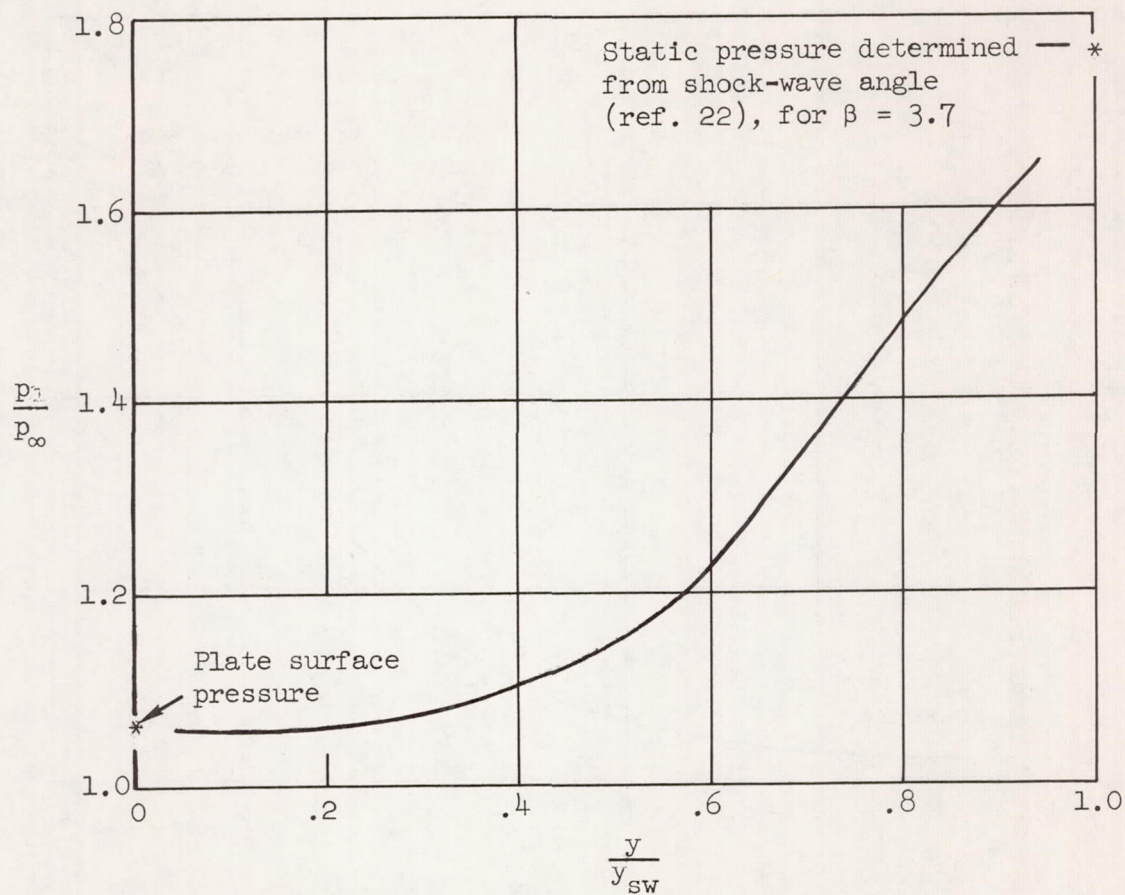
(c) Shock-wave shapes measured on flat plates with square leading edges in air at $M_\infty = 12.3$ (ref. 20).

Figure 4.- Continued.



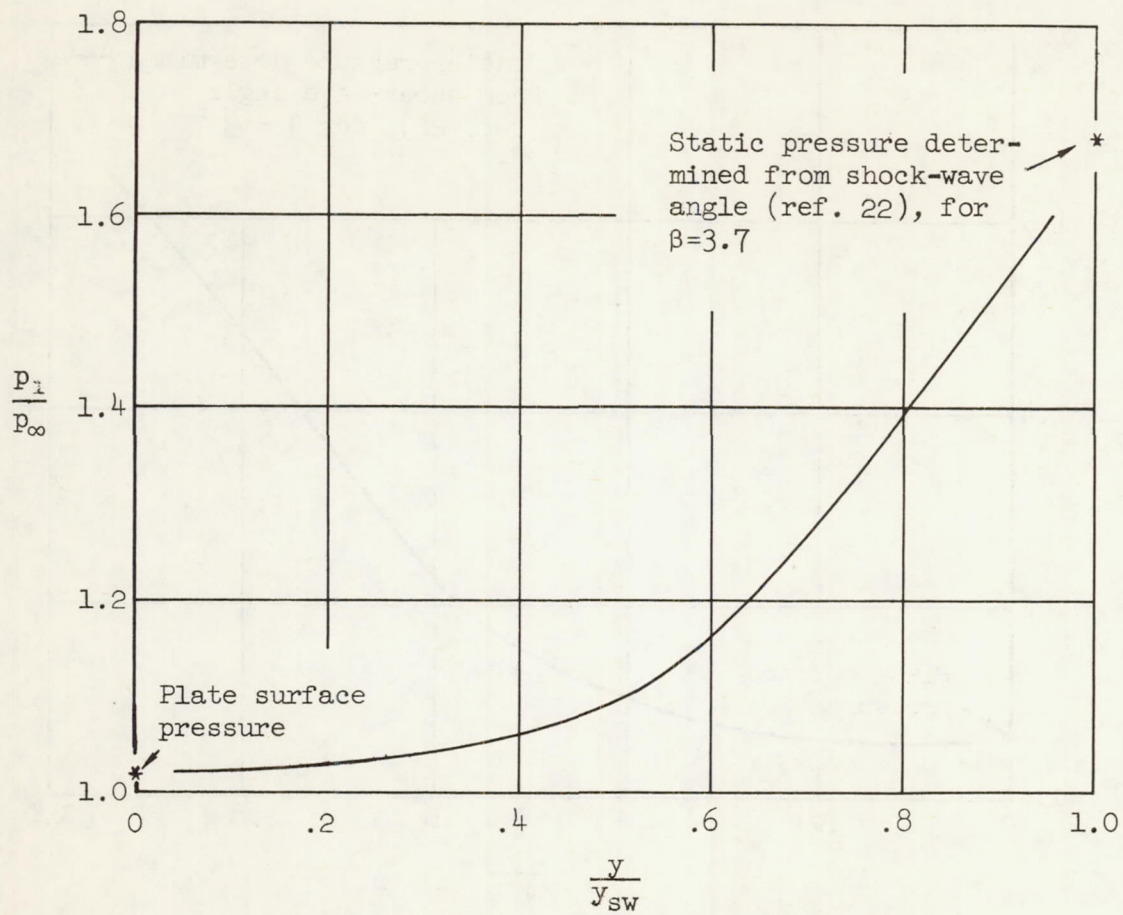
(d) Correlation with theory of measured shock-wave shapes on flat plates with square leading edges (ref. 20).

Figure 4.- Concluded.



(a) Station 5.

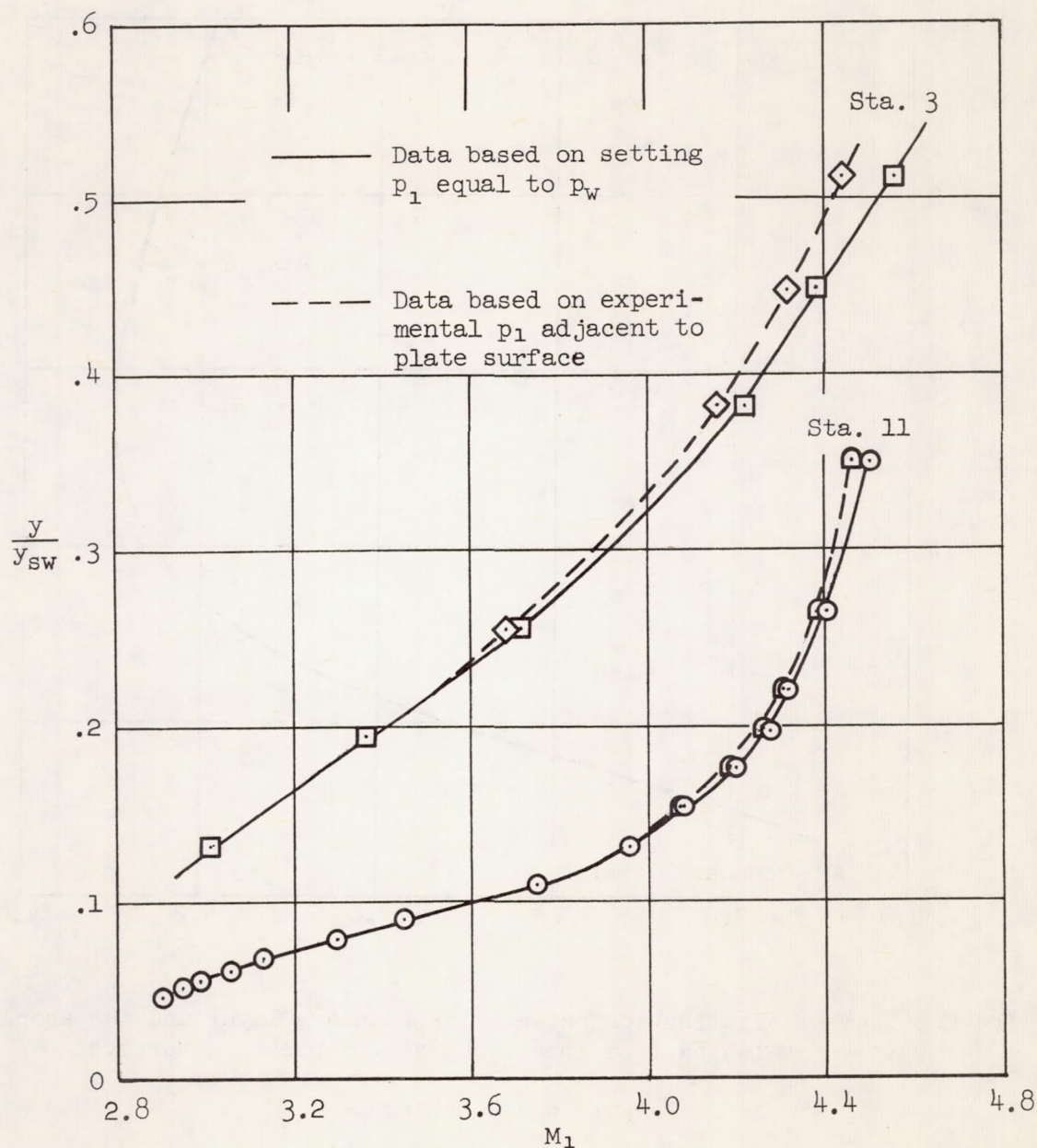
Figure 5.- Static pressure profiles measured on a flat plate with a cylindrical leading edge ($r = 0.062$ in.).



(b) Station 7.

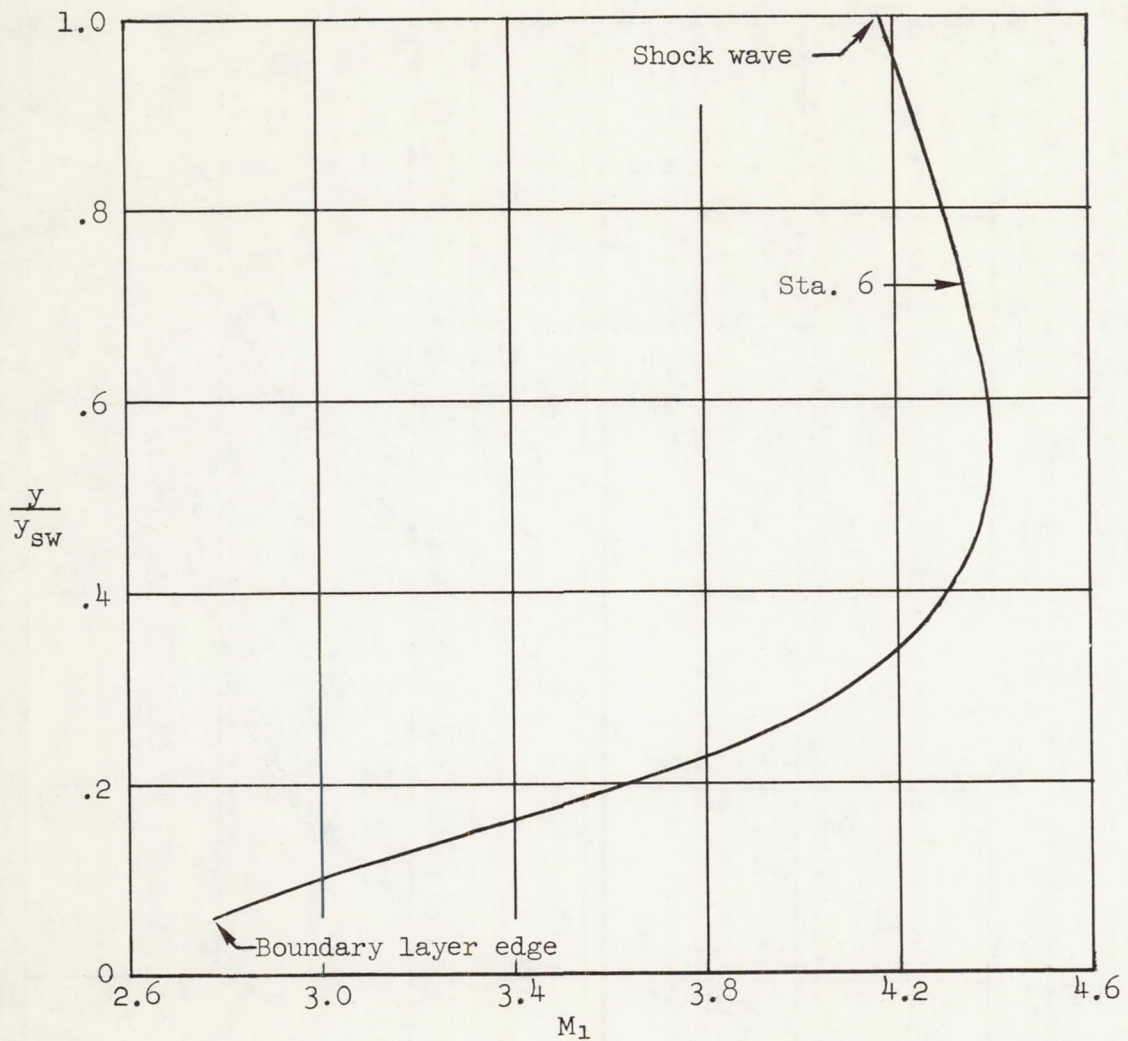
Figure 5.- Concluded.

A
3
6
6



(a) Comparison of Mach number distribution as evaluated from surface pressure or static pressure surveys.

Figure 6.- Effect of experimental static pressure normal to the plate on Mach number distribution in shear layer ($r = 0.062$ in.).



(b) Mach number distribution between the boundary layer and the shock wave as evaluated from impact and static pressure surveys.

Figure 6.- Concluded.

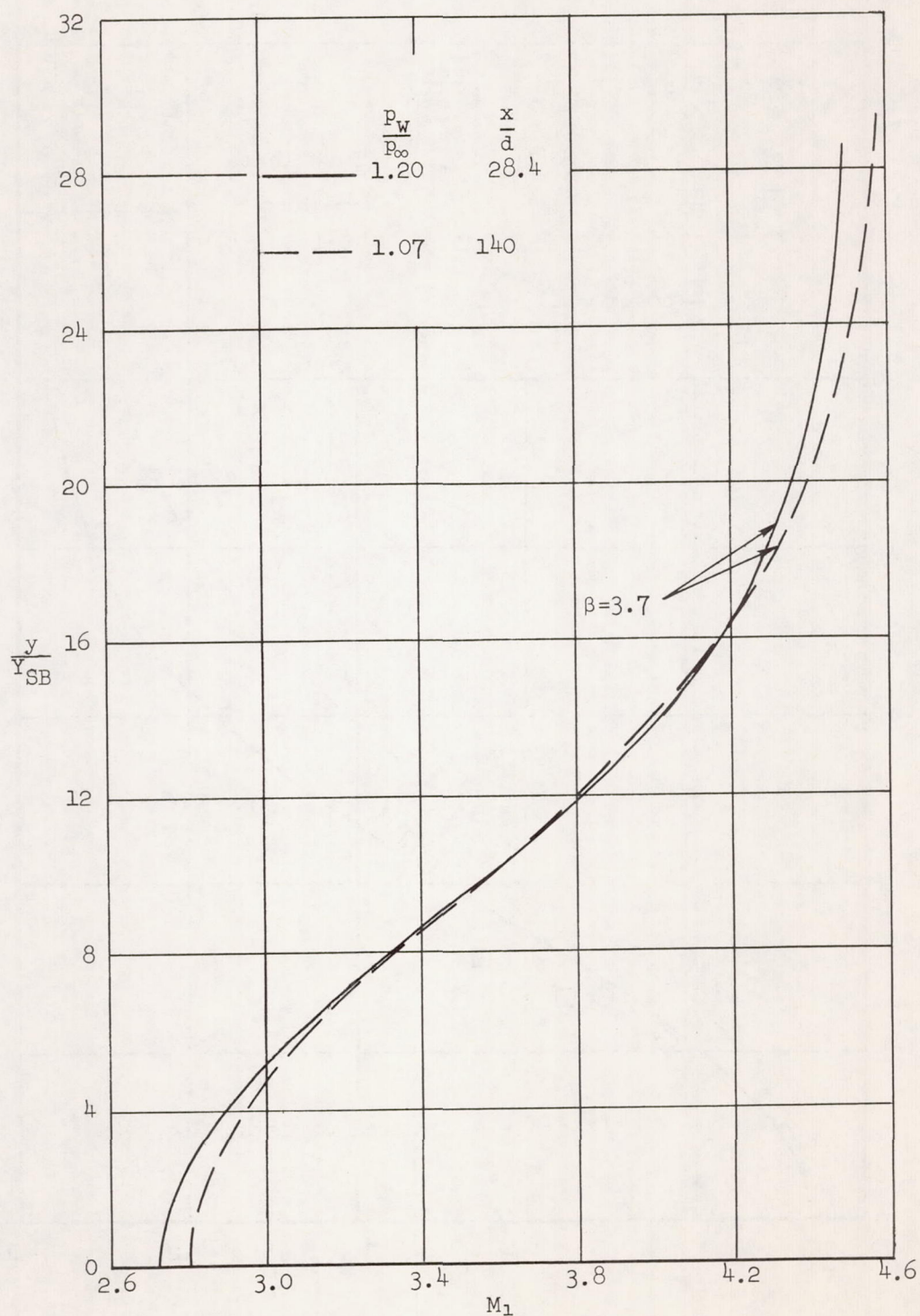
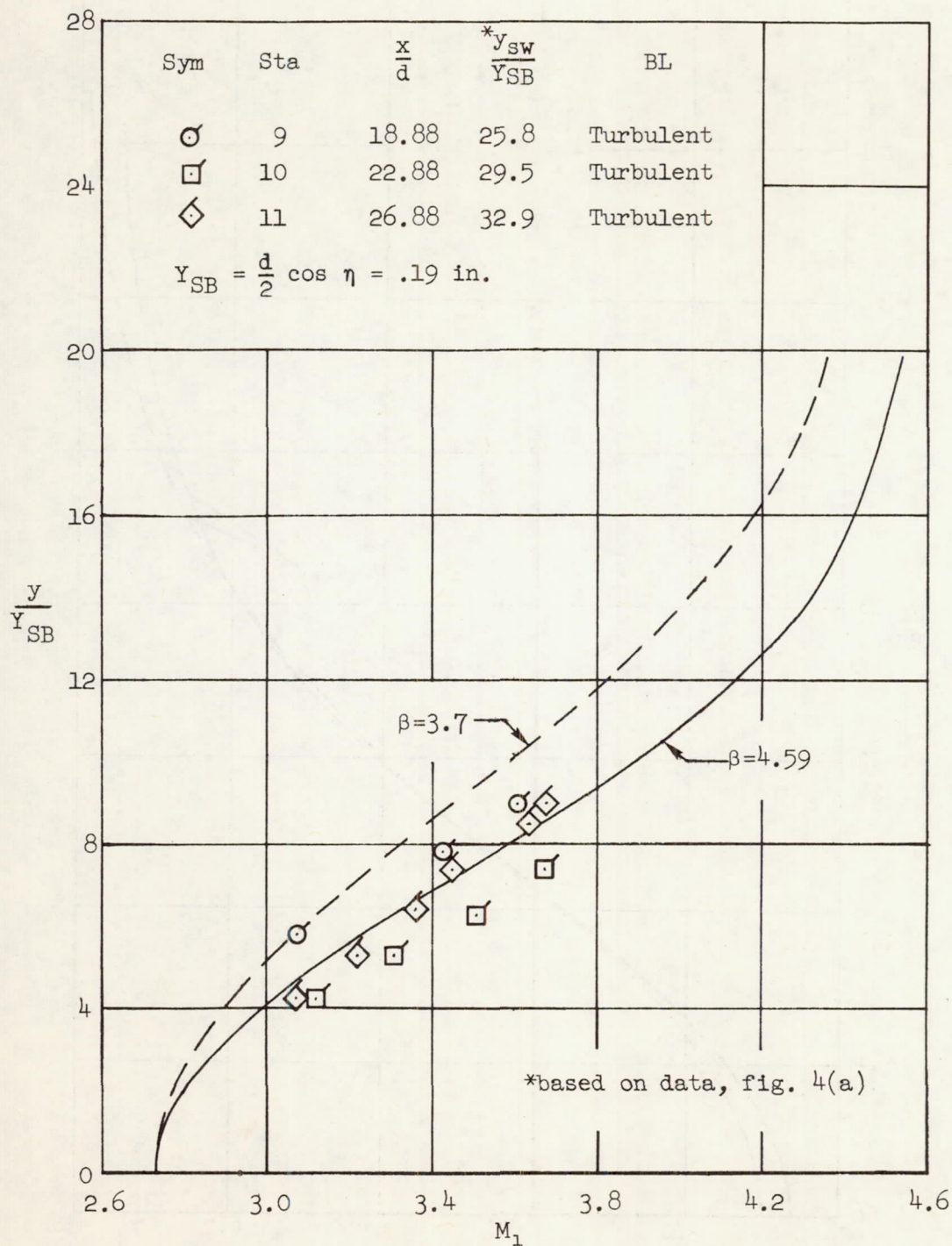
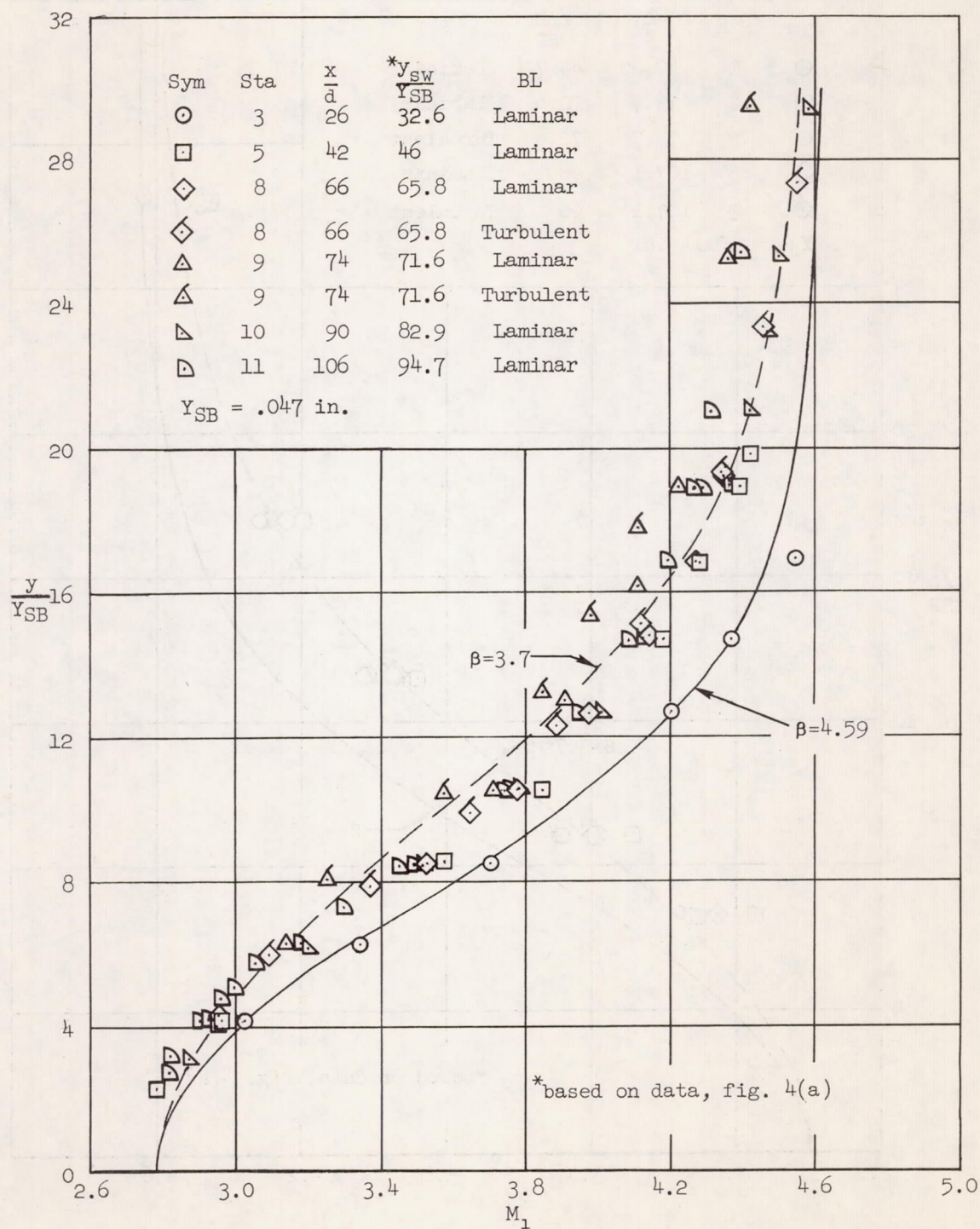


Figure 7.- The effect of surface static pressure distribution on the calculated Mach number distribution in the shear layer over the cylindrical leading-edge flat plate ($r = 0.062$ in.).



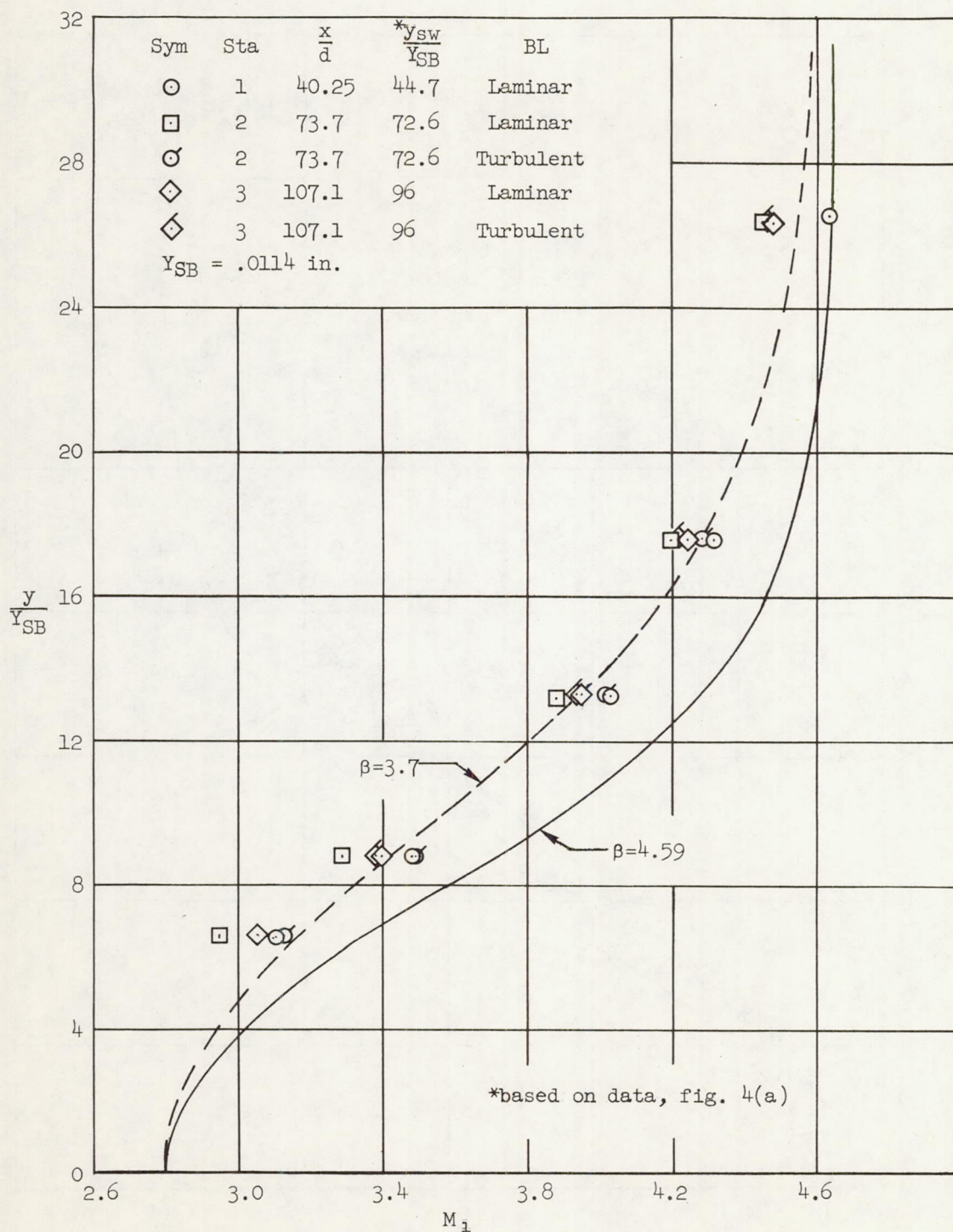
(a) 0.250-inch leading-edge radius (BL tripped).

Figure 8.- Mach number distribution in the shear layer on a flat plate with various cylindrical leading edges.



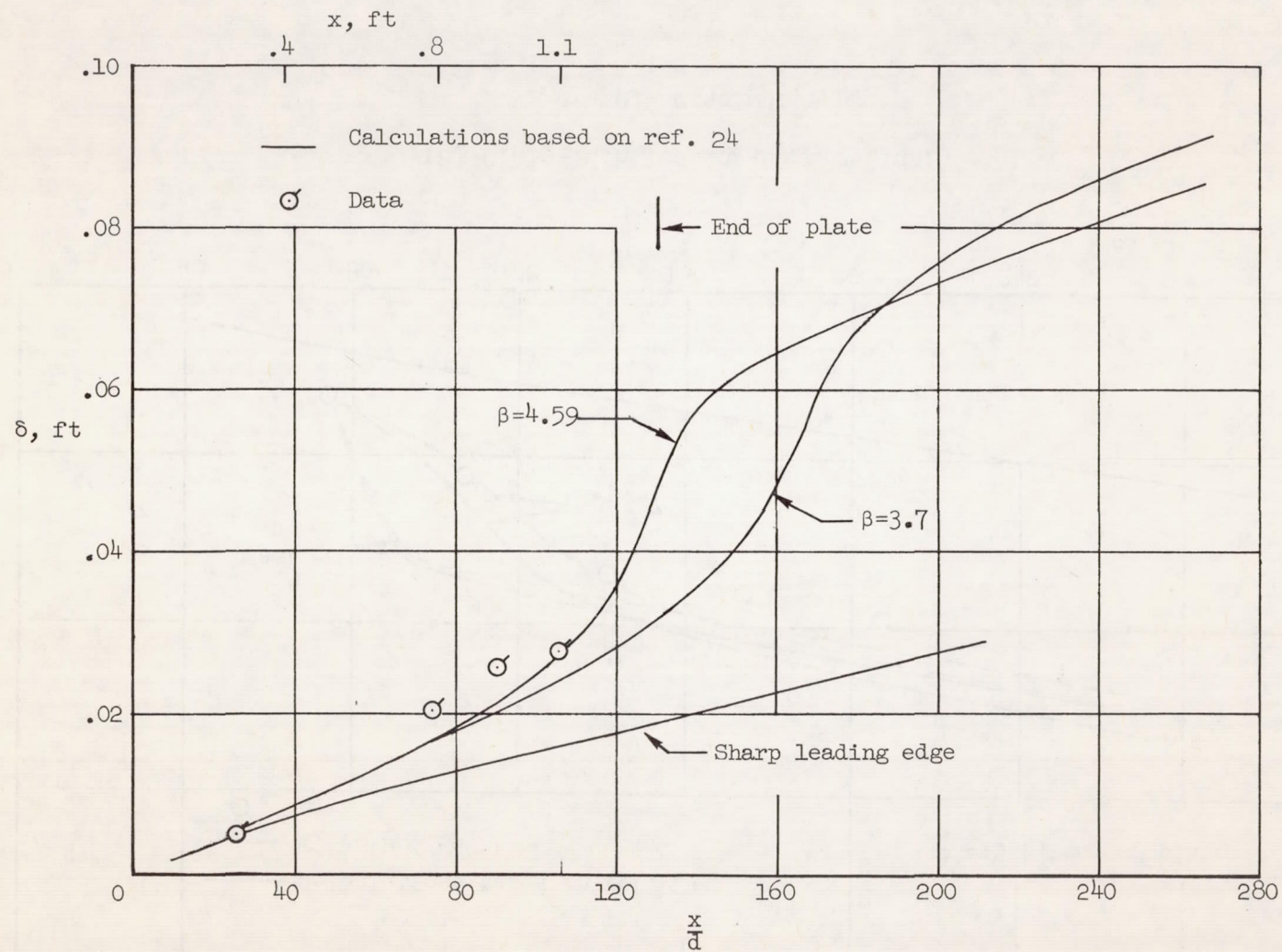
(b) 0.062-inch leading-edge radius (BL tripped for flagged symbols).

Figure 8.- Continued.



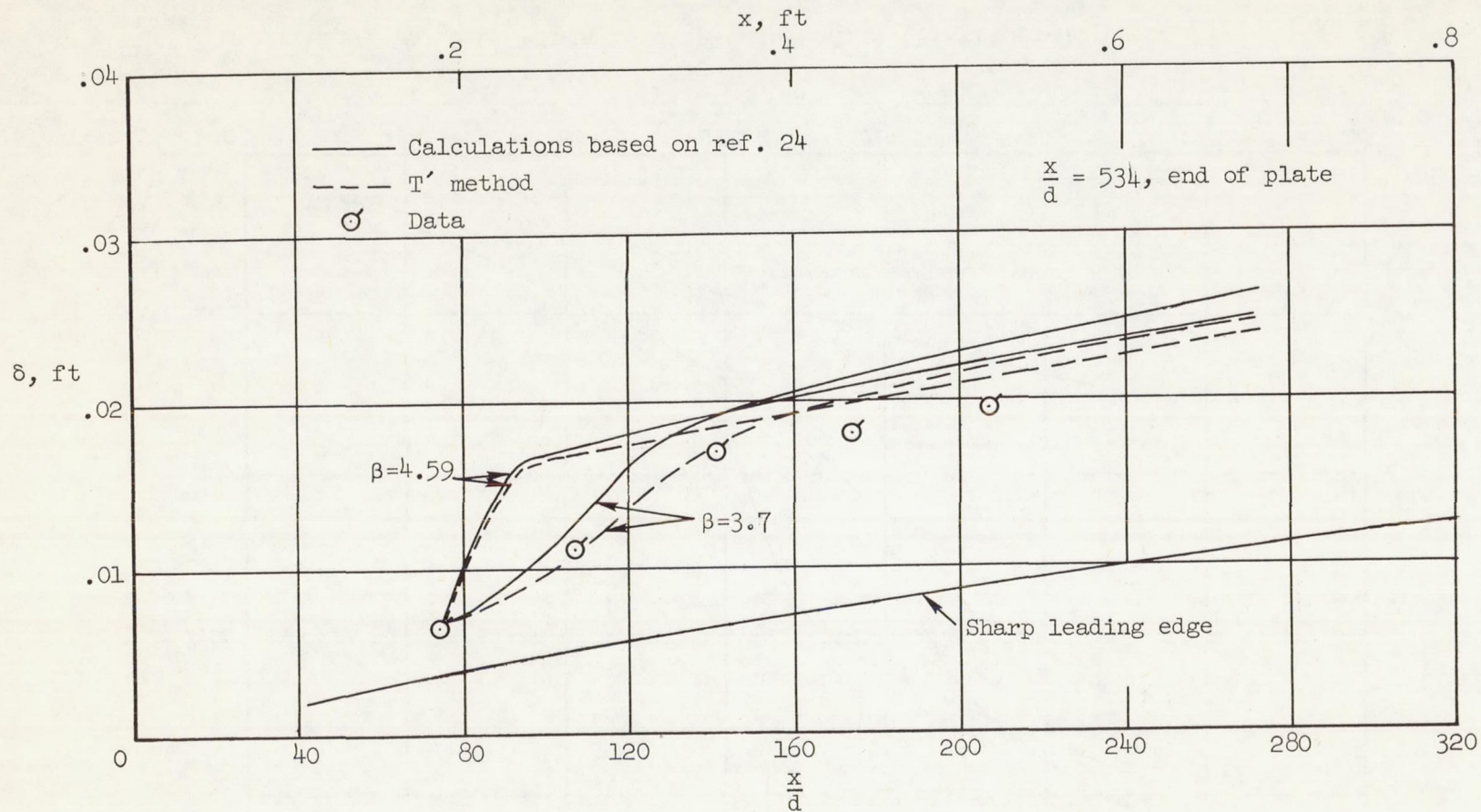
(c) 0.015-inch leading-edge radius.

Figure 8.- Concluded.



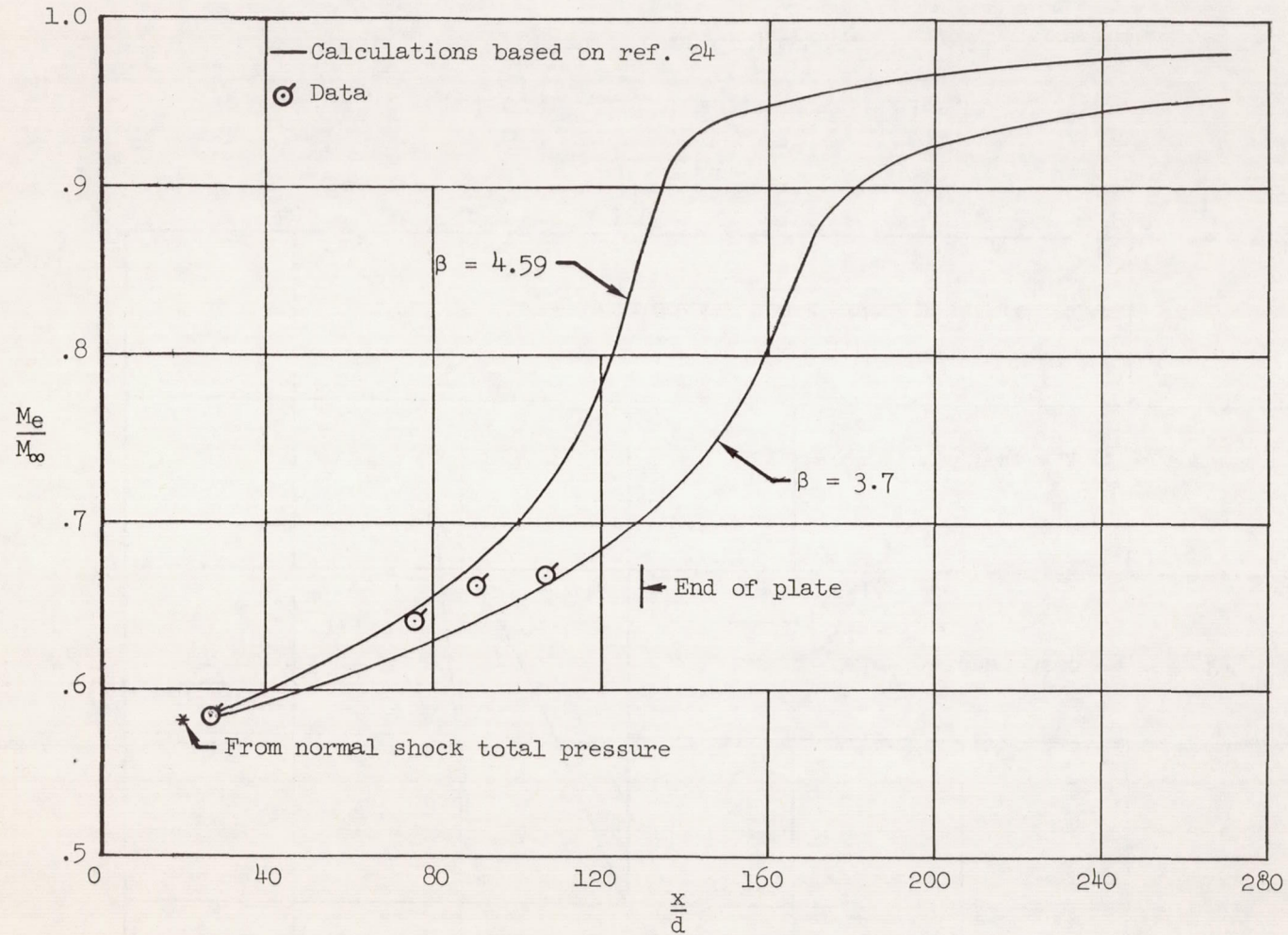
(a) 0.062-inch leading-edge radius (BL tripped).

Figure 9.- Turbulent boundary-layer growth on a flat plate with various cylindrical leading edges.



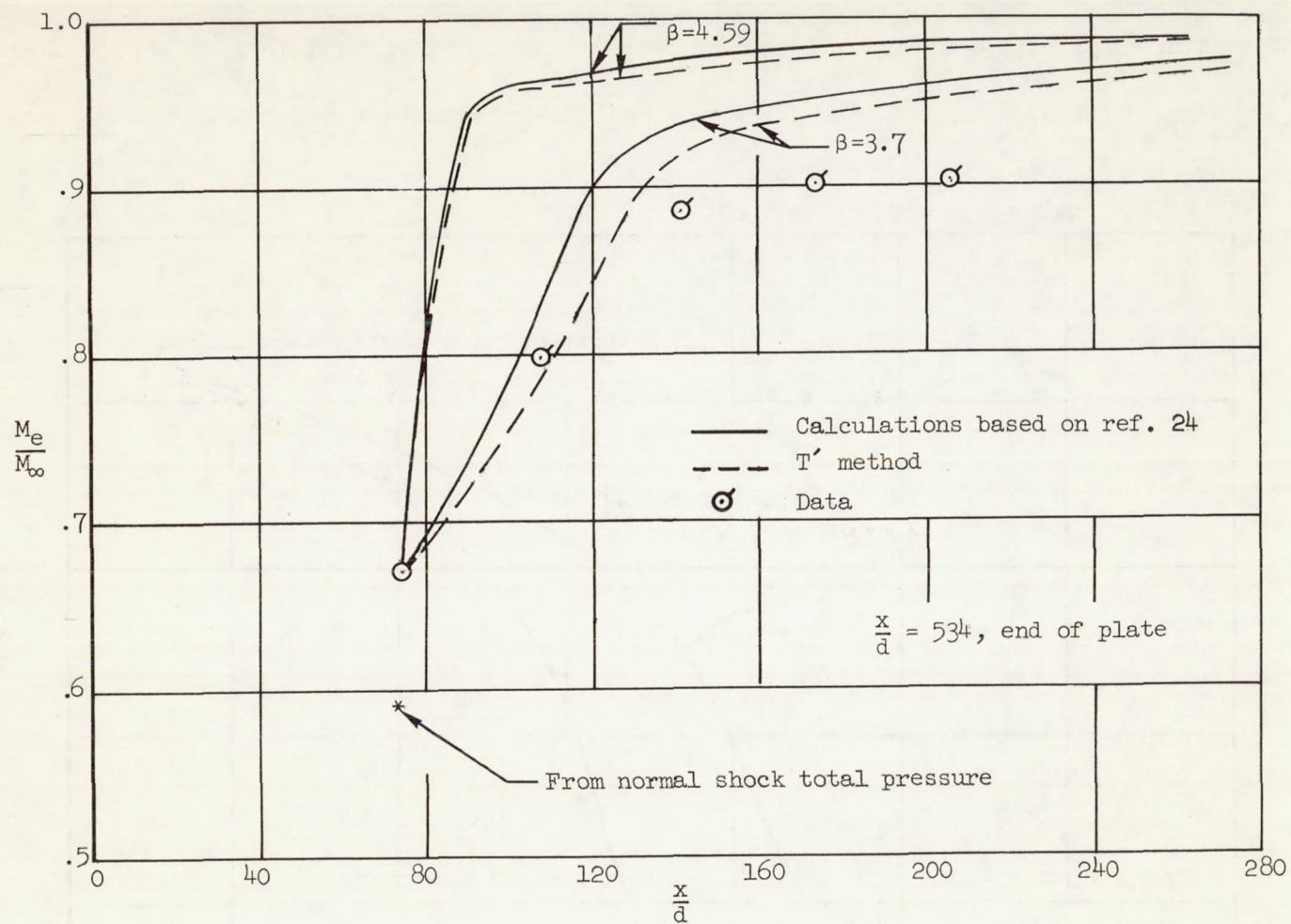
(b) 0.015-inch leading-edge radius.

Figure 9.- Concluded.



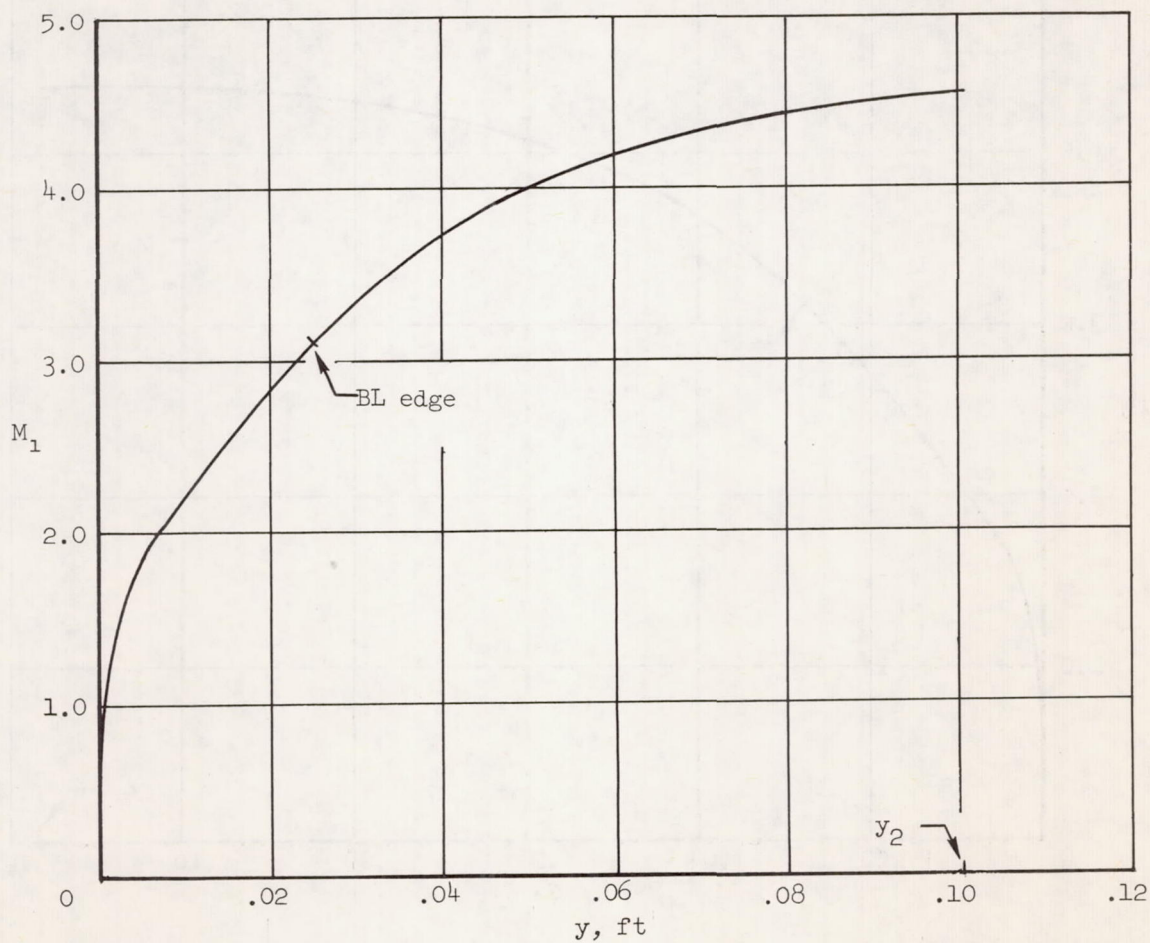
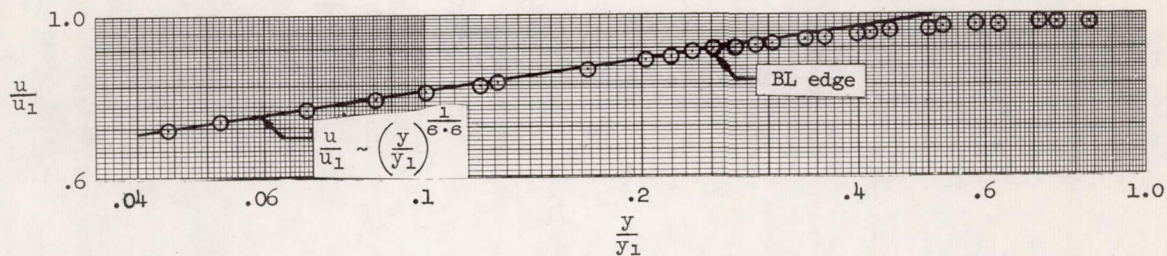
(a) 0.062-inch leading-edge radius.

Figure 10.— Mach number at the edge of the turbulent boundary layer on a flat plate with various cylindrical leading edges (BL tripped).



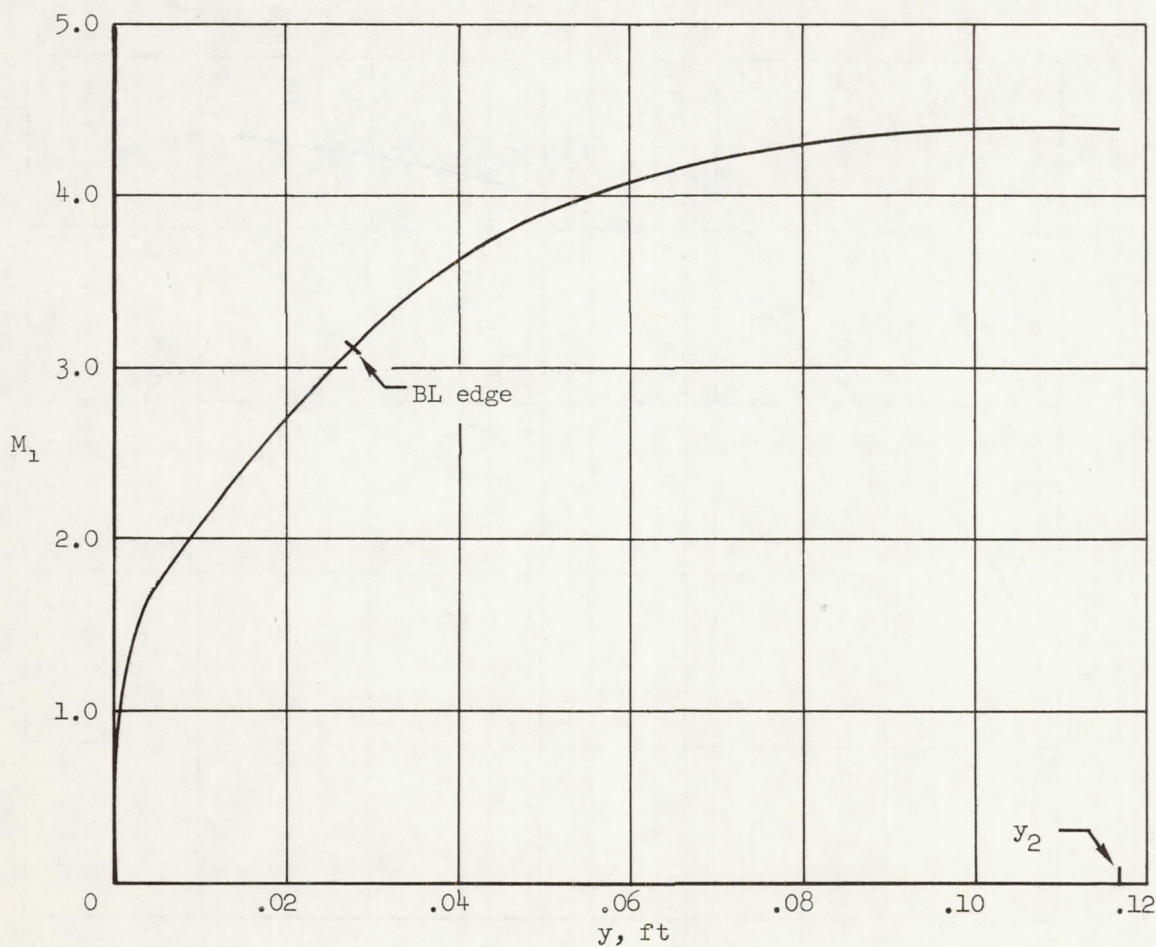
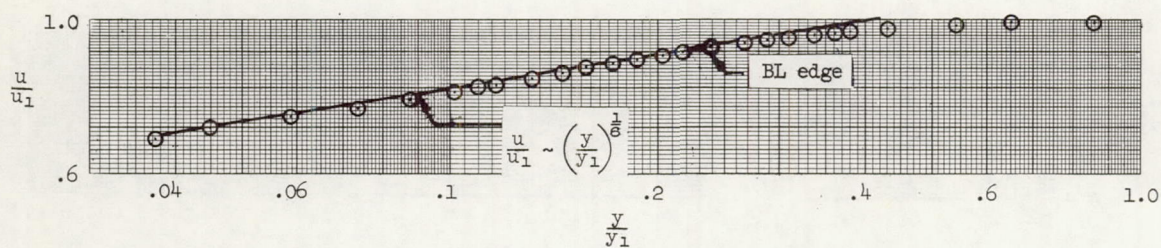
(b) 0.015-inch leading-edge radius.

Figure 10.- Concluded.



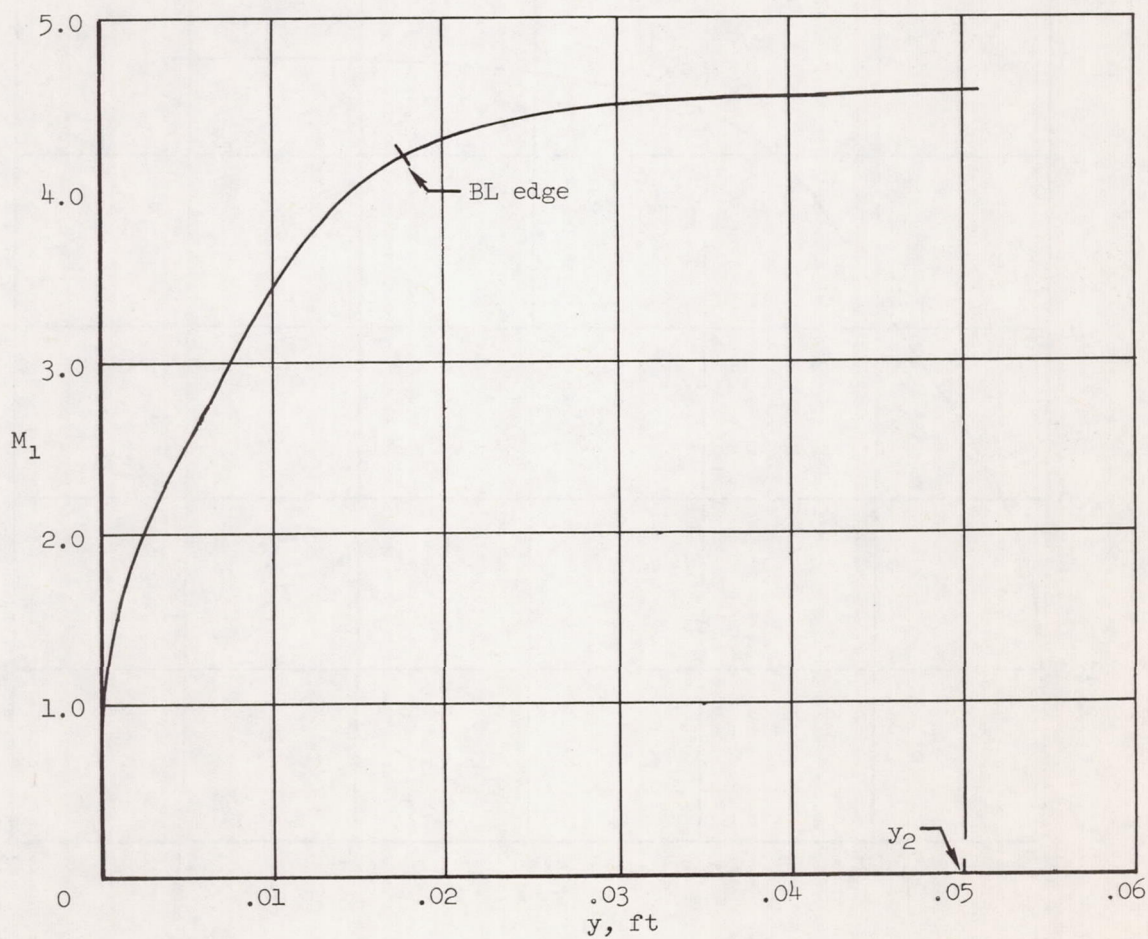
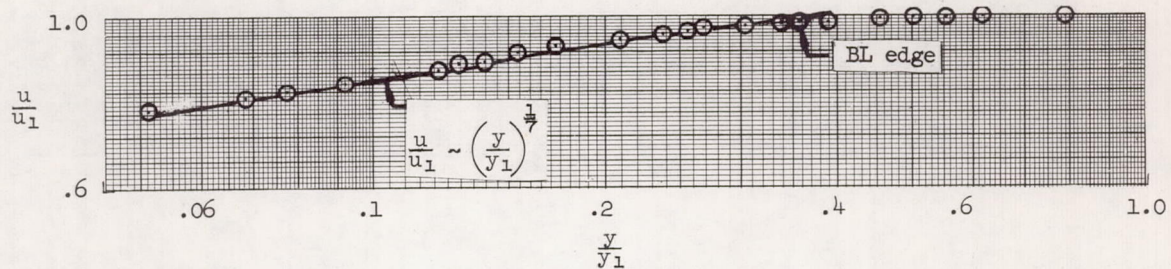
(a) 0.062-inch leading-edge radius, station 10 (BL tripped).

Figure 11.- Mach number and velocity distributions in the boundary layer on a flat plate with various cylindrical leading edges.



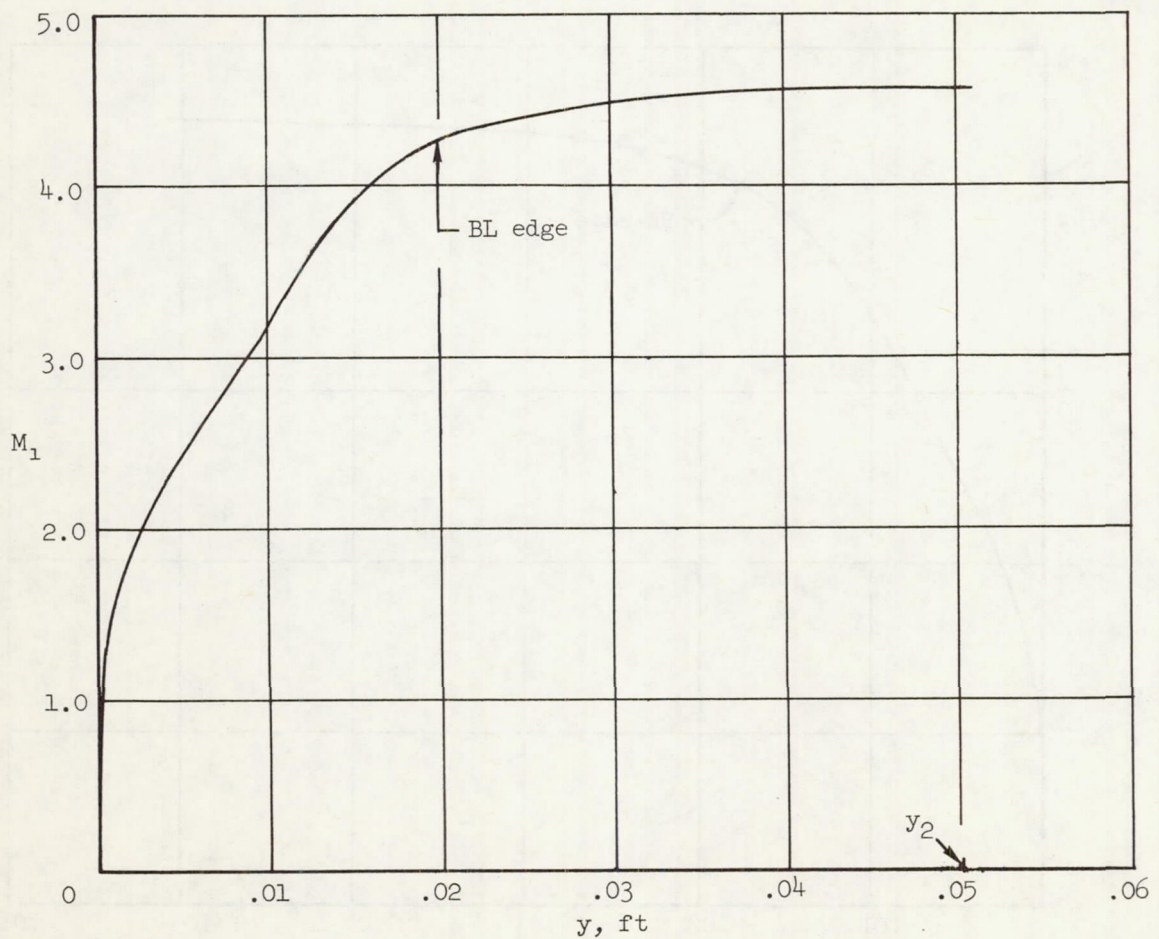
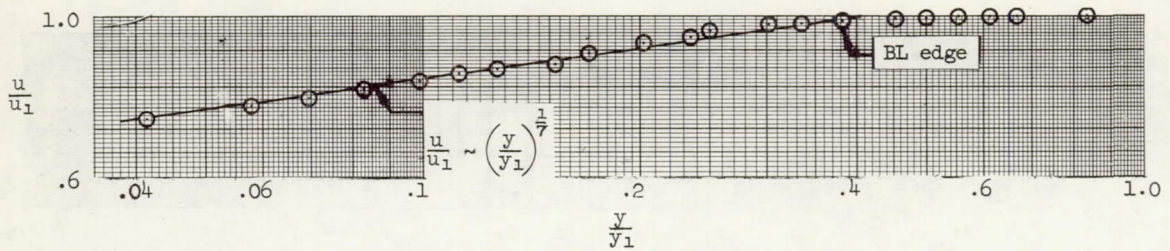
(b) 0.062-inch leading-edge radius, station 11 (BL tripped).

Figure 11.- Continued.



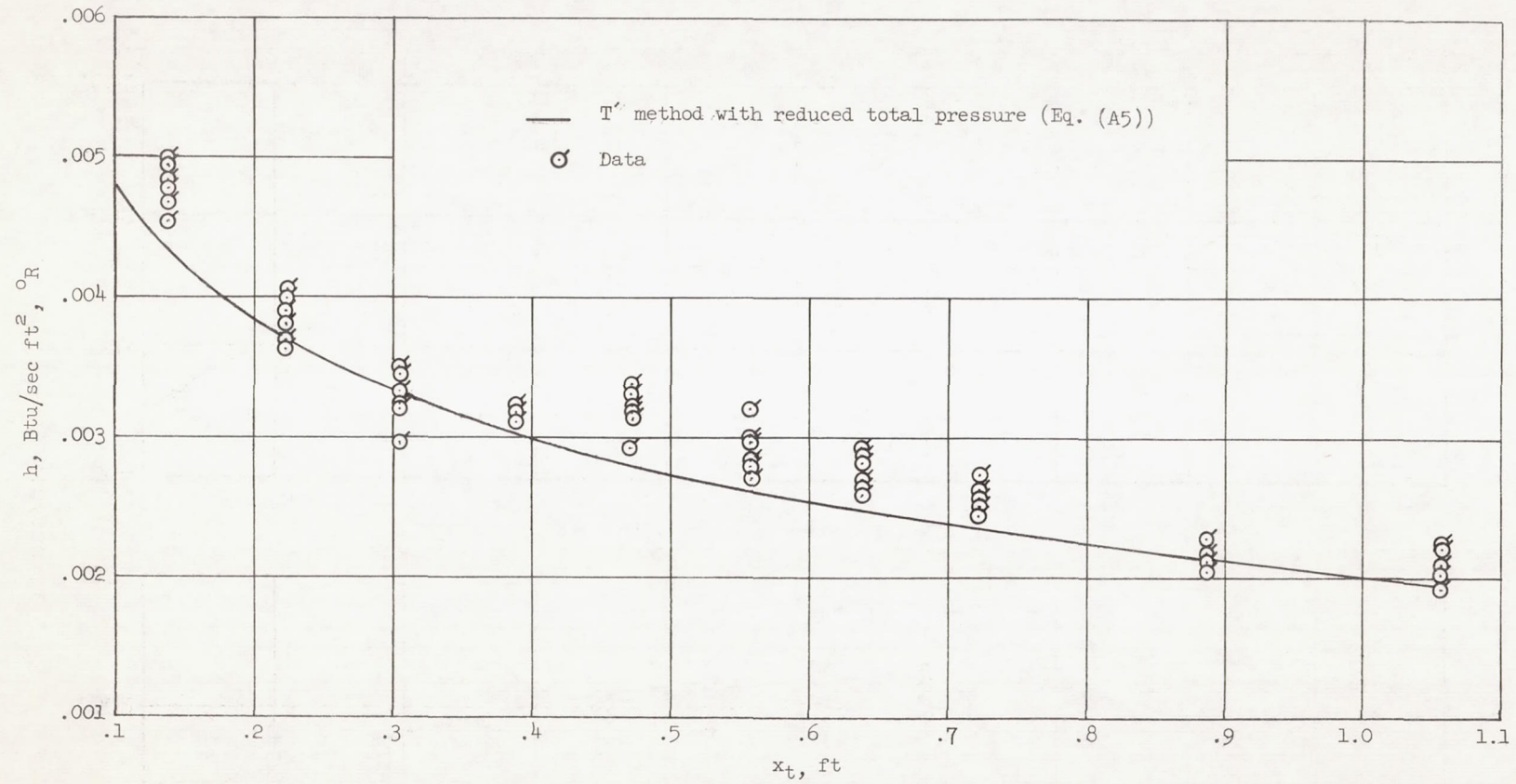
(c) 0.015-inch leading-edge radius, station 5 (no BL trip).

Figure 11.- Continued.



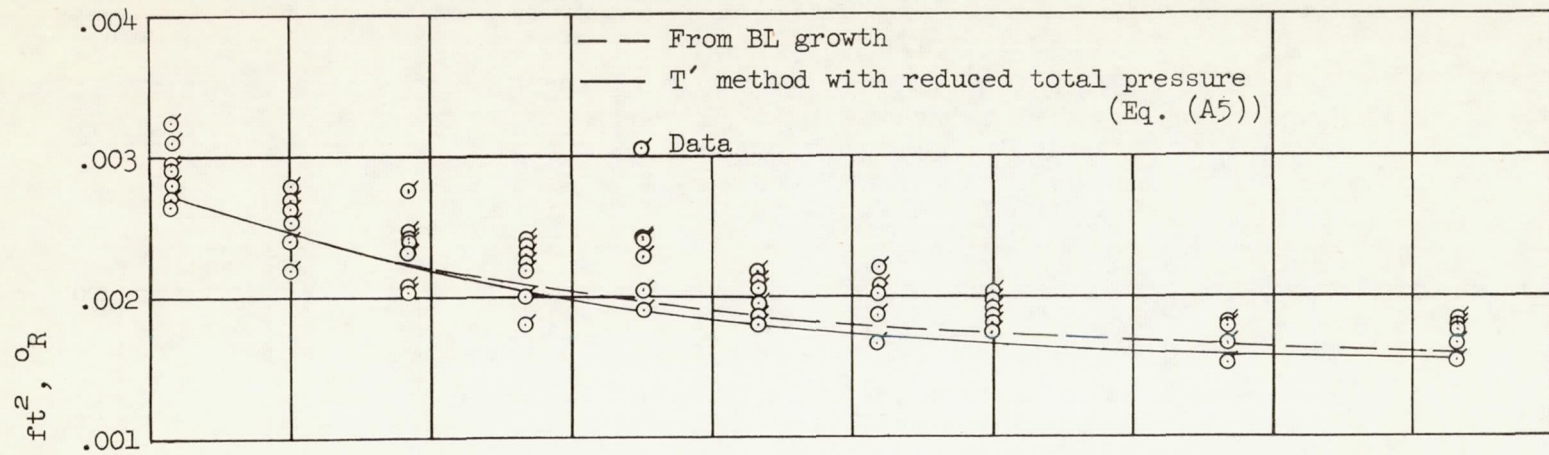
(d) 0.015-inch leading-edge radius, station 6 (no BL trip).

Figure 11.- Concluded.

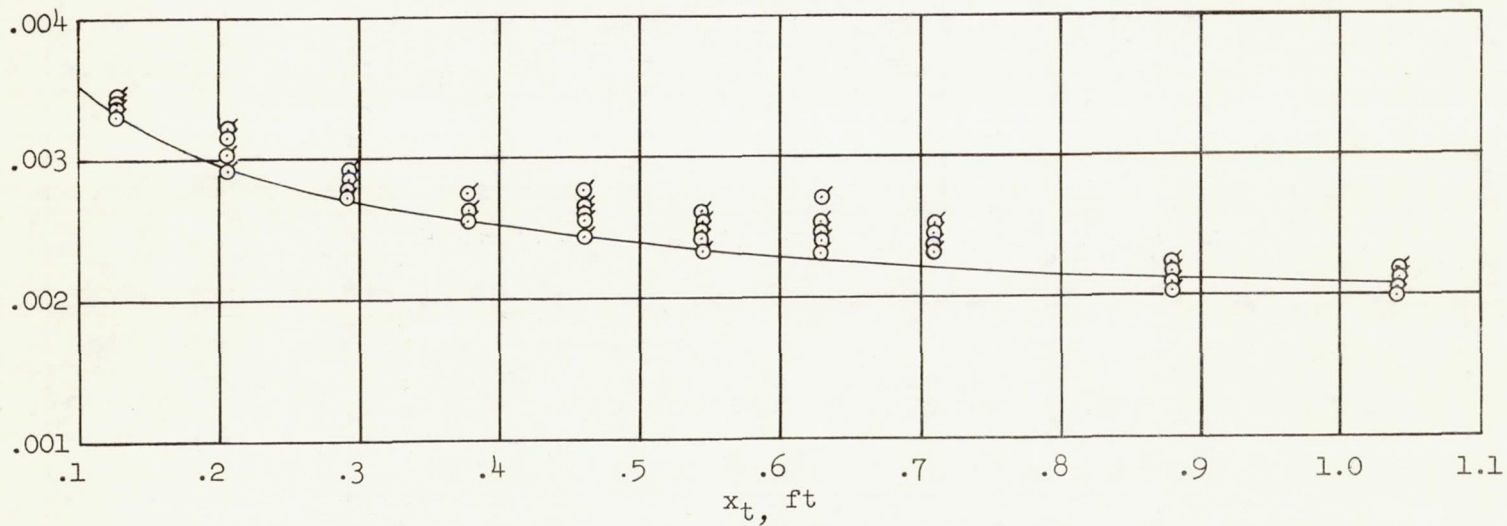


(a) 0.250-inch leading-edge radius.

Figure 12.- Turbulent heat-transfer coefficient on a flat plate with various cylindrical leading edges (BL tripped).

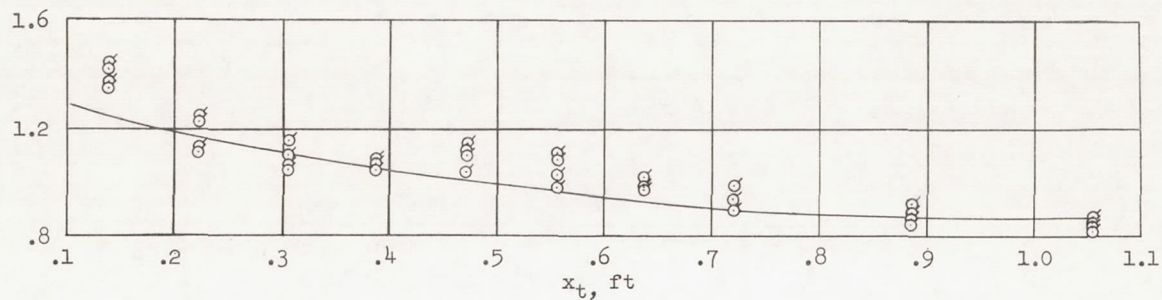


(b) 0.062-inch leading-edge radius.

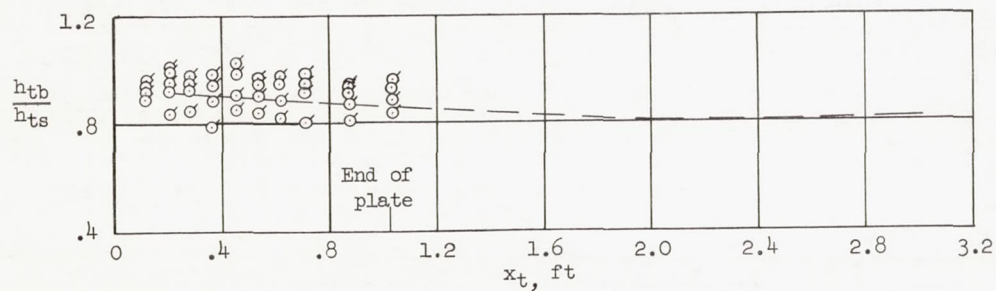


(c) 0.045-inch leading-edge radius.

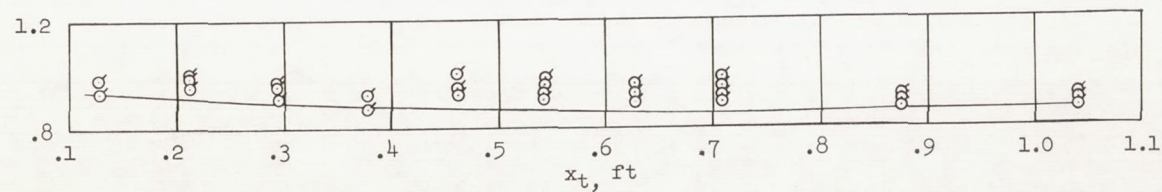
Figure 12.- Concluded.



(a) 0.250-inch leading-edge radius.



(b) 0.062-inch leading-edge radius.



(c) 0.045-inch leading-edge radius.

Figure 13.- Comparison of turbulent heat-transfer coefficients on a flat plate with various cylindrical leading edges to that calculated for a sharp leading-edged flat plate (BL tripped).